Electronic Supplementary Material (ESI) for Inorganic Chemistry Frontiers.

Electronic Supporting Information

Geometrically Isomeric Pt_2Ag_2 Acetylide Complexes of 2,6-Bis(diphenylphosphino)pyridine: Luminescent and Vapochromic Properties

Jian Quan,[a,c] Zhong-Hui Chen,[a] Xu Zhang,[a] Jin-Yun Wang,[a,*] Li-Yi Zhang,[a] and Zhong-Ning Chen[a,b,*]

[a] *State Key Laboratory of Structural Chemistry, Fujian Institute of Research on the Structure of Matter, Chinese Academy of Sciences, Fuzhou, Fujian 350002, China. E-mail: czn@fjirsm.ac.cn*

[b] *Fujian Science & Technology Innovation Laboratory for Optoelectronic Information of China, Fuzhou, Fujian 350108, China*

[c] *University of Chinese Academy of Sciences, Beijing, 100039, China*

Experimental Section

General Procedures and Materials. All operations were carried out under dry argon atmosphere by using Schlenk techniques at ambient temperature and vacuum-line system unless specified. The solvents were dried, distilled and degassed prior to use except those for spectroscopic measurements were of spectroscopic grade. Ag(tht)(SO_3CF_3), Pt(COD)Cl_2 (COD = 1,5-cycloocatadiene) and alkynl ligands were accessible by similar synthetic procedures in the literatures.[1-3] 2,6-Dichloropyridine, $AgSbF_6$, HC≡CC_6H_5, and HC≡C$C_6H_4CF_3$-4 were commercially available.

2,6-Bis(diphenylphosphino)pyridine ($(Ph_2P)_2py$). Ph_2PCl (12 mL, 65 mmol) in THF (20 mL) was added slowly to THF (100 mL) with lithium (500 mg, 72 mmol). Upon stirring for 1 h, the reaction mixture gradually turned to deep red, which was then refluxed at 70℃ for 3 h. Upon cooling down, the excess Li was removed and the deep red solution was kept at 0 °C in an ice bath. To the solution was added dropwise a THF (30 mL) solution of 2,6-dichloropyridine (4.0 g, 27 mmol). The reaction mixture was warmed to room temperature and then refluxed at 70 °C for 1 h to give a pale-yellow suspension. Upon cooling to room temperature, the solvent was removed under reduced pressure and a saturated NH_4Cl solution (60 mL) was added. The product as extracted with CH_2Cl_2 (3 ×50 mL) and the combined organic layers were washed with saturated NaCl solution (50 mL) and dried with $MgSO_4$. After concentrated under vacuum, the residue was purified by crystallization in ethanol as white solid. Yield: 80% (9.6 g). m.p.: 124-125 ℃. Anal. Calcd for $C_{29}H_{23}NP_2$: C, 77.84; H, 5.18; N, 3.13. Found: C, 77.67; H, 5.20; N, 3.09. ^{1}H NMR (400 MHz, $CDCl_3$, ppm): 7.01 (m, 3,5-py-H, 2H), 7.08-7.48 (m, 4-Py-H, C_6H_5, 21H). ^{31}P NMR (162 MHZ, $CDCl_3$, ppm): -4.09 ppm. ESI-MS: m/z 448.6 ($[M + H]^+$).

Physical Measurements. The ^{1}H and ^{31}P NMR spectra were measured on a Bruker Avance III (400 MHz) spectrometer. The UV-Vis absorption spectra were measured on a Perkin-Elmer Lambda 25 UV-vis spectrophotometer. The infrared spectra (IR) were recorded on a Magna 750 FT-IR spectrophotometer with KBr pellets. The elemental analyses (C, H, N) were carried out on a Perkin-Elmer model 240 C elemental analyzer. The electrospray ion mass spectra (ESI-MS) were recorded on a Finnigan DECAX-30000 LCQ mass spectrometer using dichloromethane/methanol as mobile phase. The emission and excitation spectra together with the emission lifetimes in various states were determined on an Edinburgh FLS920 fluorescence spectrometer. The emission quantum yield (Φ_{em}) in various states were determined by the integrating

sphere (142 mm in diameter) using an Edinburgh FLS920 Spectrofluorophotometer. The emission quantum yield (Φ_{em}) in degassed dichloromethane solution at room temperature was estimated using $[Ru(bpy)_3](PF_6)_2$ in acetonitrile as the reference standard (Φ_{em} = 0.062). Luminescence vapochromic experiments were performed upon sufficient exposure of the quartz slices to various saturated VOC vapors at ambient temperature for about 10 min. The PMMA films were made on quartz slides (2.5 cm × 4 cm) by spin-coating.

Crystal Structural Determination. Crystals suitable for X-ray crystallographic measurement were grown by layering n-heptane onto the corresponding solutions. Single crystals were measured on Rigaku Saturn 70 CCD or Bruker D8 VENTURE diffractometer by the ω scan technique at room temperature using graphite-monochromated Mo-Ka (λ = 0.71073 A˚) radiation. The CrystalClear or APEX III software package was used for data reduction and empirical absorption correction. The structures were solved by direct method and the heavy atoms were located from E-map. The remaining non-hydrogen atoms were determined from the successive difference Fourier syntheses. The non-hydrogen atoms were refined with anisotropic thermal parameters. The hydrogen atoms were generated geometrically with isotropic thermal parameters. The structures were refined on F^2 by full-matrix least-squares method using the SHELXTL-97 program package.[4] In the crystal structure of **2b**·2.5MeCN, the solvate molecules were treated as a diffuse contribution to the overall scattering without specific atom positions by SQUEEZE/PLATON due to severe disorder of these solvate molecules in the lattices. The number of solvate molecules of crystal **2b**·2.5MeCN was calculated by void volume and residual electron density in crystal lattice, and further confirmed by weight loss according to thermogravimetry-mass spectrometry (TG-MS) analysis.

Computational Methodology. All the calculations were performed in Gaussian 09 program package.[5] Firstly, the geometrical structures as isolated molecules of **2b** in the ground state (G_0) and **1b**, **2b** and **4b** in the lowest-energy triplet state (T_1) were optimized, respectively, by the restricted and unrestricted density functional theory (DFT) method with the B3LYP functional.[6] The initial structures were extracted from the crystal structural parameters by X-ray crystallography. Then, in order to analyze the spectroscopic properties, 80 singlet (for **2b** based on the optimized G_0 structure) and 6 triplet (for **1b**, **2b** and **4b** on the optimized T_1 structures) excited states of these complexes were calculated by time-dependent DFT (TD-DFT) method[7-9] with the same functional used in the optimization process. The solvent effects of CH_2Cl_2 was included by using the

polarizable continuum model method (PCM).[10,11] To understand deeply the emission properties of **2b** with different intramolecular conformations, the calculations of triplet excited state were also implemented for **2b**·3CH_2Cl_2 and **2b**·2.5MeCN on the basis of the crystal structural data without geometrical optimization. In these calculations, the Stuttgart-Dresden (SDD) basis set and the effective core potentials (ECPs)[12] were used to describe the Pt and Ag atoms, while other non-metal atoms of P, F, O, N, C and H were described by the all-electron basis set of 6-31G**. Visualization of the frontier molecular orbitals were performed by GaussView. The contributions of fragments to orbitals in the electronic excitation process were analysed by the Ros & Schuit method[13] (C-squared population analysis method, SCPA) in Multiwfn 3.8 program.[14]

Table S1. Crystallographic Data for cis-Pt_2Ag_2 Complexes **2a** and **3a** and trans-Pt_2Ag_2 Complexes **1b**·$4CH_2Cl_2$, **2b**, **2b**·$3CH_2Cl_2$, **2b**·2.5MeCN and **4b**.

	2a·$11/4CH_2Cl_2$	**3a**·$5/2CH_2Cl_2$	**1b**·$4CH_2Cl_2$	**2b**	**2b**·$3CH_2Cl_2$	**2b**·5/2MeCN	**4b**
chemical formula	$C_{94.75}H_{71.5}Ag_2Cl_{5.5}F_6N_2O_6P_4Pt_2S_2$	$C_{98.5}H_{67}Ag_2Cl_5F_{18}N_2O_6P_4Pt_2S_2$	$C_{108}H_{98}Ag_2Cl_8F_6N_2O_{18}P_4Pt_2S_2$	$C_{92}H_{66}Ag_2F_6N_2O_6P_4Pt_2S_2$	$C_{95}H_{72}Ag_2Cl_6F_6N_2O_6P_4Pt_2S_2$	$C_{97}H_{73.5}Ag_2F_6N_{4.5}O_6P_4Pt_2S_2$	$C_{100}H_{58}Ag_2F_{30}N_2O_6P_4Pt_2S_2$
formula weight	2436.93	2687.71	2903.40	2203.38	2458.16	2306.02	2747.40
Crystal system	orthorhombic	triclinic	triclinic	orthorhombic	monoclinic	monoclinic	monoclinic
space group	*Pbca*	$P\bar{1}$	$P\bar{1}$	*C*2221	$P2_1/c$	$P2_1/n$	$P2_1/c$
T (K)	293(2)	293(2)	293(2)	293(2)	100(2)	150(2)	298(2)
a (Å)	13.6978(10)	21.242(3)	14.5178(2)	19.271(2)	14.8764(6)	13.9577(10)	27.930(4)
b (Å)	27.641(2)	25.331(3)	15.031(2)	19.620(2)	41.6942(17)	25.4328(17)	13.1649(16)
c (Å)	50.357(4)	25.716(4)	16.7816(3)	22.773(3)	16.0997(6)	25.5005(14)	26.744(4)
α (°)		117.242(6)	115.005(4)				
β (°)		94.361(11)	111.540(7)		116.1220(10)	102.251(2)	104.657(2)
γ (°)		109.512(8)	92.567(6)				
V (Å^3)	19066(3)	11155(3)	2998.87(17)	14245	8966.0(6)	8846.1(10)	9514(2)
Z	8	4	1	4	4	4	4
density (g/cm^3)	1.698	1.600	1.608	1.700	1.821	1.731	1.918
μ (mm^{-1})	3.660	3.139	2.984	3.878	3.907	3.779	3.565
R_{int}	0.0406	0.1229	0.0342	0.0558	0.362	0.0792	0.0435
R_1[a] [I>2σ(I)]	0.0524	0.0820	0.0438	0.0352	0.0741	0.0483	0.0374
wR_2[b] [I>2σ(I)]	0.1416	0.2084	0.1252	0.0898	0.1724	0.1105	0.1128
GOF	1.083	1.023	1.042	1.036	1.169	1.039	0.849

[a] $R_1 = \Sigma||F_o|-|F_c||/\Sigma|F_o|$, [b] $wR_2 = [\Sigma w(|F_o|-|F_c|)^2/\Sigma w|F_o|^2]^{1/2}$.

Table S2. Selected Interatomic Distances (Å) and Bond Angles (°)for cis-Pt_2Ag_2 Complexes **2a** and **3a** and trans-Pt_2Ag_2 Complexes **2b**, **2b**·$3CH_2Cl_2$ and **2b**·2.5MeCN.

2a·$11/4CH_2Cl_2$		**3a**·$5/2CH_2Cl_2$		**2b**		**2b**·$3CH_2Cl_2$		**2b**·5/2MeCN	
Pt1-Ag1	3.1251(6)	Pt1-Ag1	3.0975(11)	Pt1-Ag1	2.9648(6)	Pt1-Ag1	2.9352(7)	Pt1-Ag1	3.0862(6)
Pt1-Ag2	3.0607(6)	Pt1-Ag2	3.0606(11)			Pt1-Ag2	2.9942(8)	Pt1-Ag1a	3.1521(6)
Pt2-Ag1	3.0811(6)	Pt2-Ag1	3.2940(12)	Pt2-Ag1	2.9992(6)	Pt2-Ag1	3.0587(8)	Pt2-Ag2	3.0349(6)
Pt2-Ag2	2.9921(6)	Pt2-Ag2	2.9298(11)			Pt2-Ag2	2.9873(8)	Pt2-Ag2a	3.0500(6)
Ag1-Ag2	3.0234(8)	Ag1-Ag2	3.0611(15)						
Pt1-C59	2.011(6)	Pt1-C117	2.036(10)	Pt1-C30	2.013(6)	Pt1-C59	2.001(9)	Pt1-C1	2.005(6)
Pt1-C67	2.004(6)	Pt1-C126	1.990(11)			Pt1-C67	2.008(9)	Pt1-C9	1.997(6)
Pt1-P1	2.3290(15)	Pt1-P1	2.342(3)	Pt1-P1	2.3082(16)	Pt1-P1	2.307(2)	Pt1-P1	2.3097(16)
Pt1-P3	2.3314(15)	Pt1-P3	2.307(3)			Pt1-P2	2.313(2)	Pt1-P2	2.3156(16)
Pt2-C75	2.019(6)	Pt2-C135	2.003(11)	Pt2-C38	2.006(7)	Pt2-C75	1.994(9)	Pt2-C46	2.008(6)
Pt2-C83	2.006(6)	Pt2-C144	2.031(14)			Pt2-C83	2.024(10)	Pt2-C54	2.002(5)
Pt2-P2	2.3229(15)	Pt2-P2	2.321(3)	Pt2-P2	2.3063(18)	Pt2-P3	2.311(2)	Pt2-P3	2.3162(14)
Pt2-P4	2.3062(14)	Pt2-P4	2.320(3)			Pt2-P4	2.311(2)	Pt2-P4	2.3077(14)
Ag1-C67	2.281(6)	Ag1-C117	2.270(7)	Ag1-C30	2.290(5)	Ag1-C59	2.323(9)	Ag1-C1	2.301(5)
Ag1-C75	2.254(6)	Ag1-C135	2.282(10)	Ag1-C38	2.359(7)	Ag1-C75	2.296(9)	Ag1-C9	2.288(5)
Ag2-C59	2.259(6)	Ag2-C126	2.324(7)	Ag2-C83	2.329(9)	Ag2-C67	2.338(9)	Ag2-C46	2.346(5)
Ag2-C83	2.322(6)	Ag2-C144	2.341(8)					Ag2-C54	2.341(5)
Ag2-N2	2.626(5)	Ag2-N2	2.379(8)						
C67-Pt1-P3	170.37(17)	C117-Pt1-P3	173.9(3)	C30-Pt1-C30a	175.3(3)	C59-Pt1-C67	167.7(4)	C1-Pt1-C9	169.7(2)
C59-Pt1-P1	174.78(17)	C126-Pt1-P1	169.5(3)	P1-Pt1-P1a	171.14(8)	P1-Pt1-P2	172.32(8)	P1-Pt1-P2	170.82(5)
C75-Pt2-P4	176.84(18)	C135-Pt2-P4	175.4(3)	C38-Pt2-C38	164.7(4)	C75-Pt2-C83	170.5(4)	C54-Pt2-C46	167.0(2)
C83-Pt2-P2	170.61(16)	C144-Pt2-P2	169.6(2)	P2-Pt2-P2a	170.73(9)	P3-Pt2-P4	168.90(8)	P4-Pt2-P3	171.98(5)
C75-Ag1-C67	174.1(2)	C117-Ag1-C135	156.2(3)	C30-Ag1-C38	161.7(2)	C75-Ag1-C59	165.9(3)	C9-Ag1-C1	168.4(2)
C59-Ag2-C83	153.2(2)	C126-Ag2-C144	127.8(3)			C83-Ag2-C67	163.7(3)	C54-Ag2-C46	154.64(19)
C59-Ag2-N2	90.24(17)	C126-Ag2-N2	112.3(3)						
C83-Ag2-N2	112.20(18)	C144-Ag2-N2	117.5(4)						

Table S3. The Partial Molecular Orbital Compositions (%) by SCPA Approach (C-squared Population Analysis Proposed by Ros & Schuit) in the Ground State and Absorption Transitions for cis-Pt_2Ag_2 complex **2a** in CH_2Cl_2 Solution Calculated by the TD-DFT Method at the B3LYP Level.

orbital	energy (eV)	MO contribution (%)			
		Pt (s/p/d)	Ag (s/p/d)	C≡CC_6H_5	$(Ph_2P)_2$py
LUMO	-2.60	19.60 (30/58/13)	19.88 (47/49/4)	38.35	22.17
HOMO	-6.50	11.42 (2/5/93)	31.18 (48/4/48)	53.45	3.95
HOMO-1	-6.73	15.30 (16/9/74)	14.48 (41/15/44)	64.05	6.18
HOMO-3	-6.91	24.58 (10/4/86)	16.75 (58/11/31)	53.06	5.61

state	*E*, nm (eV)	O.S.	transition (contrib.)	assignment	measured (nm)
S_1	373 (3.32)	0.2274	HOMO→LUMO (96%)	^{1}MC/^{1}IL/^{1}LLCT	359
S_2	350 (3.54)	0.2566	HOMO-1→LUMO (92%)	^{1}MC/^{1}IL/^{1}LLCT	340
S_5	330 (3.76)	0.2639	HOMO-3→LUMO (92%)	^{1}MC/^{1}IL/^{1}LLCT	

Table S4. The Partial Molecular Orbital Compositions (%) by SCPA Approach in the Lowest-Energy Triplet State and Emission Transitions for for cis-Pt_2Ag_2 complex **2a** in CH_2Cl_2 Solution Calculated by TD-DFT Method at the B3LYP Level.

orbital	energy (eV)	MO contribution (%)			
		Pt (s/p/d)	Ag (s/p/d)	C≡CC_6H_5	$(Ph_2P)_2$py
LUMO	-3.07	24.63 (14/30/56)	12.67 (64/29/7)	32.81	29.89
HOMO	-6.19	23.29 (9/6/85)	18.42 (5/9/86)	51.96	6.34
H-1	-6.55	9.33 (5/9/87)	27.12 (45/12/44)	58.93	4.62
H-2	-6.69	13.90 (11/9/80)	13.71 (36/22/41)	66.37	6.02
H-3	-6.89	17.18 (10/8/81)	17.52 (57/11/32)	58.91	6.39

state	*E*, nm (eV)	O.S.	transition (contrib.)	assignment	measured (nm)
T_1	646 (1.92)	0.0000	HOMO→LUMO (83%)	^{3}MC/^{3}IL/^{3}LLCT	642
T_2	456 (2.72)	0.0000	H-1→LUMO (51%)	^{3}MC/^{3}IL/^{3}LLCT	
			H-2→LUMO (9%)	^{3}IL/^{3}MC/^{3}LLCT/^{3}LMCT	
T_3	446 (2.78)	0.0000	H-3→LUMO (46%)	^{3}MC/^{3}IL/^{3}LLCT	

Table S5. The Partial Molecular Orbital Compositions (%) by SCPA Approach (C-squared Population Analysis Proposed by Ros & Schuit) in the Ground State and Absorption Transitions for for trans-Pt_2Ag_2 complex **2b** in CH_2Cl_2 Solution Calculated by the TD-DFT Method at the B3LYP Level.

orbital	energy (eV)	MO contribution (%)			
		Pt (s/p/d)	Ag (s/p/d)	C≡CC_6H_5	$(Ph_2P)_2$py
LUMO+6	-1.80	17.86 (46/15/39)	14.39 (92/6/1)	7.46	60.29
LUMO+1	-2.29	17.32 (37/30/32)	6.10 (68/23/9)	8.78	67.80
LUMO	-2.91	29.69 (43/23/34)	10.33 (46/48/6)	23.27	36.71
HOMO	-6.41	21.90 (0/6/94)	28.29 (64/3/34)	47.65	2.15
HOMO-1	-6.48	30.19 (0/3/97)	6.01 (13/46/41)	61.67	2.14
HOMO-3	-6.99	20.53 (39/3/58)	19.26 (38/9/53)	53.95	6.26
HOMO-4	-7.14	66.99 (27/1/72)	7.21 (4/1/95)	10.62	15.17

state	*E*, nm (eV)	O.S.	transition (contrib.)	assignment	measured (nm)
S_1	424 (2.92)	0.0272	HOMO→LUMO (96%)	^{1}MC/^{1}LLCT/^{1}IL	
S_2	419 (2.96)	0.4510	HOMO-1→LUMO (94%)	^{1}LLCT/^{1}MC/^{1}IL	397
S_4	361 (3.43)	0.1354	HOMO-4→LUMO (72%)	^{1}MC/^{1}MLCT/^{1}IL	
			HOMO-3→LUMO (18%)	^{1}MC/^{1}LLCT/^{1}IL	
S_7	350 (3.54)	0.0922	HOMO→LUMO+1 (75%)	^{1}LLCT/^{1}MLCT/^{1}MC	
S_{26}	307 (4.03)	0.1570	HOMO→LUMO+6 (61%)	^{1}LLCT/^{1}MC/^{1}MLCT	319

Table S6. The Molecular Orbital Compositions (%) by SCPA Approach in the Lowest-Energy Triplet State and Emission Transitions for trans-Pt_2Ag_2 complex **2b** in CH_2Cl_2 Solution TD-DFT Method at the B3LYP Level.

orbital	energy (eV)	MO Contribution (%)			
		Pt (s/p/d)	Ag (s/p/d)	C≡CC_6H_5	$(Ph_2P)_2$py
LUMO+1	-2.44	31.77 (37/19/45)	3.12 (30/38/31)	23.34	41.76
LUMO	-3.40	31.96 (43/24/33)	17.56 (76/20/4)	19.35	31.12
HOMO	-5.93	27.16 (0/3/97)	16.09 (3/8/88)	55.56	1.19
HOMO-1	-6.49	19.64 (0/4/96)	27.88 (67/20/13)	50.77	1.72
HOMO-2	-6.69	32.84 (27/7/66)	13.42 (0/5/95)	44.23	9.51

state	*E*, nm (eV)	O.S.	transition (contrib.)	assignment	measured (nm)
T_1	661 (1.87)	0.0000	HOMO→LUMO (94%)	^{3}MC/^{3}LLCT/^{3}IL	643
T_2	567 (2.19)	0.0000	HOMO-1→LUMO (71%)	^{3}MC/^{3}LLCT/^{3}IL	
			HOMO→LUMO+1 (18%)	^{3}MC/^{3}LLCT/^{3}IL	
T_3	528 (2.35)	0.0000	HOMO-2→LUMO (84%)	^{3}MC/^{3}LLCT/^{3}IL	

Table S7. The Partial Molecular Orbital Compositions (%) by SCPA Approach in the Lowest-Energy Triplet State and Emission Transitions for trans-Pt_2Ag_2 complex **1b** in CH_2Cl_2 Solution Calculated by TD-DFT Method at the B3LYP Level.

orbital	energy (eV)	MO contribution (%)			
		Pt (s/p/d)	Ag (s/p/d)	C≡C$C_6H_2(OMe)_3$-3,4,5	$(Ph_2P)_2$py
LUMO	-3.31	31.77 (44/24/32)	16.48 (76/20/4)	19.67	32.08
HOMO	-5.48	13.13 (1/3/96)	8.68 (14/16/69)	77.09	1.10
HOMO-1	-5.68	7.14 (17/17/66)	19.66 (80/13/7)	72.18	1.02
HOMO-2	-6.11	8.42 (20/19/62)	13.08 (71/9/20)	76.13	2.38

state	*E*, nm (eV)	O.S.	transition (contrib.)	assignment	measured (nm)
T_1	712 (1.74)	0.0000	HOMO→LUMO (92%)	^{3}LLCT/^{3}LMCT/^{3}MC	705
T_2	581 (2.13)	0.0000	HOMO-1→LUMO (88%)	^{3}LLCT/^{3}MC/^{3}LMCT	
T_3	564 (2.20)	0.0000	HOMO-2→LUMO (76%)	^{3}LLCT/^{3}LMCT/^{3}MC	

Table S8. The Partial Molecular Orbital Compositions (%) by SCPA Approach in the Lowest-Energy Triplet State and Emission Transitions for trans-Pt_2Ag_2 complex **4b** in CH_2Cl_2 Solution Calculated by TD-DFT Method at the B3LYP Level.

orbital	energy (eV)	MO contribution (%)			
		Pt (s/p/d)	Ag (s/p/d)	C≡C$C_6H_3(CF_3)_2$-2,4	$(Ph_2P)_2$py
LUMO+1	-2.79	20.22 (31/26/44)	4.77 (34/39/28)	52.09	22.91
LUMO	-3.60	32.88 (48/26/26)	20.50 (82/15/4)	22.16	24.46
HOMO	-6.37	28.83 (0/5/95)	18.42 (7/11/82)	51.79	0.97
HOMO-1	-6.92	21.76 (0/4/96)	19.34 (57/19/23)	55.62	3.29
HOMO-2	-6.99	31.90 (21/6/73)	10.68 (1/3/96)	45.60	11.82
HOMO-3	-7.10	38.25 (18/3/79)	14.44 (7/3/90)	35.95	11.36

state	*E*, nm (eV)	O.S.	transition (contrib.)	assignment	measured (nm)
T_1	602 (2.06)	0.0000	HOMO→LUMO (92%)	^{3}MC/^{3}LLCT/^{3}IL	584
T_2	538 (2.30)	0.0000	HOMO-1→LUMO (60%)	^{3}MC/^{3}IL/^{3}LLCT/^{3}LMCT	
			HOMO→LUMO+1 (29%)	^{3}IL/^{3}MLCT/^{3}MC	
T_3	512 (2.42)	0.0000	HOMO-2→LUMO (67%)	^{3}MC/^{3}IL/^{3}LLCT/^{3}LMCT	
			HOMO-3→LUMO (18%)	^{3}MC/^{3}IL/^{3}LLCT	

Table S9. The Partial Molecular Orbital Compositions (%) by SCPA Approach in the Lowest-Energy Triplet State and Emission Transitions for Crystal **2b**·3CH_2Cl_2 Calculated by TD-DFT Method at the B3LYP Level.

orbital	energy (eV)	MO contribution (%)			
		Pt (s/p/d)	Ag (s/p/d)	C≡CC_6H_5	$(Ph_2P)_2$py
LUMO	-6.26	34.99 (51/33/16)	16.79 (68/25/6)	14.72	33.51
HOMO	-9.54	25.89 (0/5/95)	15.08 (17/25/58)	55.55	3.49
HOMO-1	-9.75	17.72 (1/7/92)	25.95 (61/7/32)	53.03	3.30
HOMO-2	-10.03	13.21 (24/11/65)	13.56 (41/7/52)	64.25	8.98

state	*E*, nm (eV)	O.S.	transition (contrib.)	assignment
T_1	510 (2.43)	0.0000	HOMO→LUMO (90%)	^{3}MC/^{3}LLCT/^{3}IL/
T_2	468 (2.65)	0.0000	HOMO-1→LUMO (83%)	^{3}MC/^{3}LLCT/^{3}IL
T_3	418 (2.97)	0.0000	HOMO-2→LUMO (78%)	^{3}MC/^{3}LLCT/^{3}LMCT

Table S10. The Partial Molecular Orbital Compositions (%) by SCPA Approach in the Lowest-Energy Triplet State and Emission Transitions for Crystal **2b**·2.5MeCN Calculated by TD-DFT Method at the B3LYP Level.

orbital	energy (eV)	MO Contribution (%)			
		Pt (s/p/d)	Ag (s/p/d)	C≡CC_6H_5	$(Ph_2P)_2$py
LUMO	-6.48	29.63 (36/37/27)	14.59 (72/24/4)	14.72	41.06
HOMO	-9.55	22.11 (2/1/97)	14.10 (7/18/74)	60.50	3.30
HOMO-1	-9.78	9.89 (7/14/78)	5.20 (1/24/75)	75.11	9.80
HOMO-3	-9.99	17.02 (19/6/75)	21.01 (67/13/19)	59.04	2.93

state	*E*, nm (eV)	O.S.	transition (contrib.)	assignment
T_1	550 (2.25)	0.0000	HOMO→LUMO (90%)	^{3}LLCT/^{3}MC/^{3}IL
T_2	471 (2.63)	0.0000	HOMO-1→LUMO (93%)	^{3}LLCT/^{3}LMCT/^{3}MC/^{3}IL
T_3	457 (2.71)	0.0000	HOMO-3→LUMO (80%)	^{3}LLCT/^{3}MC/^{3}IL

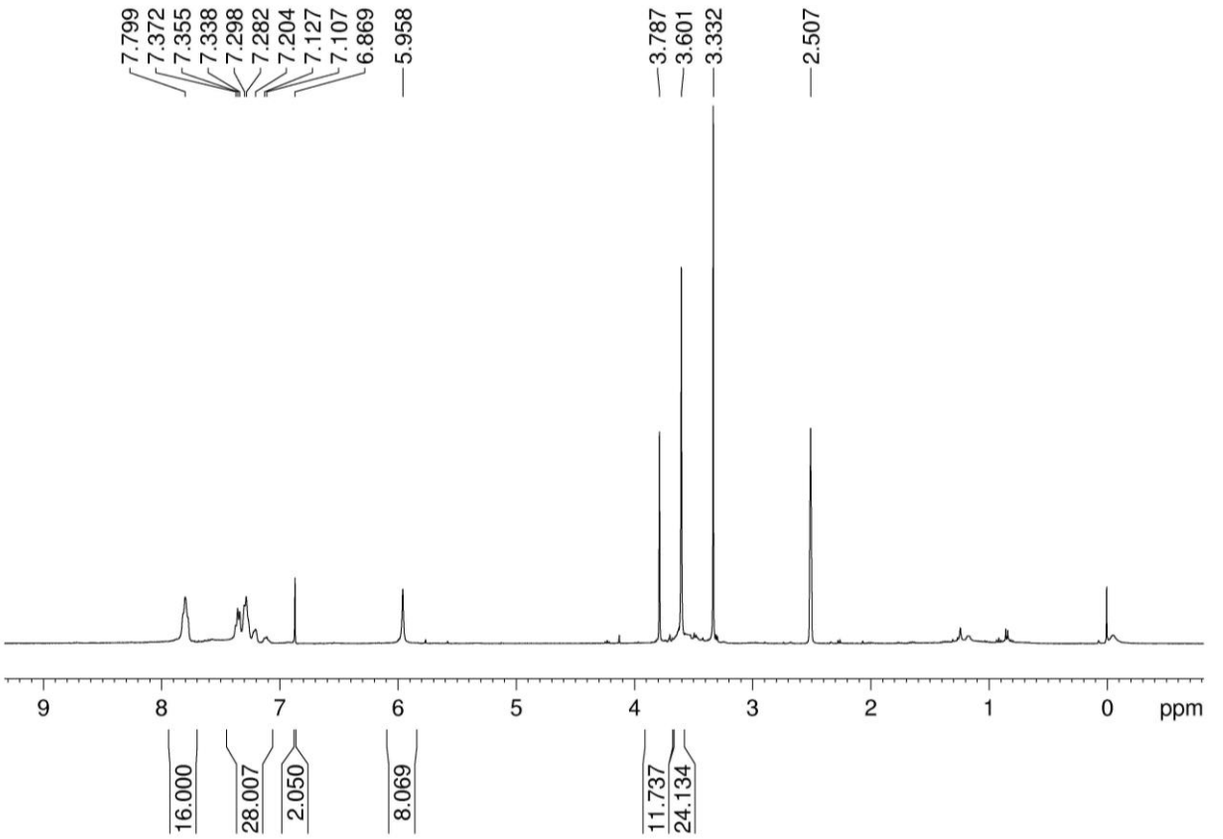

Fig. S1 ^{1}H NMR (400 MHz) spectrum of cis-[Pt_2{$(Ph_2P)_2py$}$_2${$C{\equiv}CC_6H_2(OMe)_3$-3,4,5}$_4$] in d_6-DMSO.

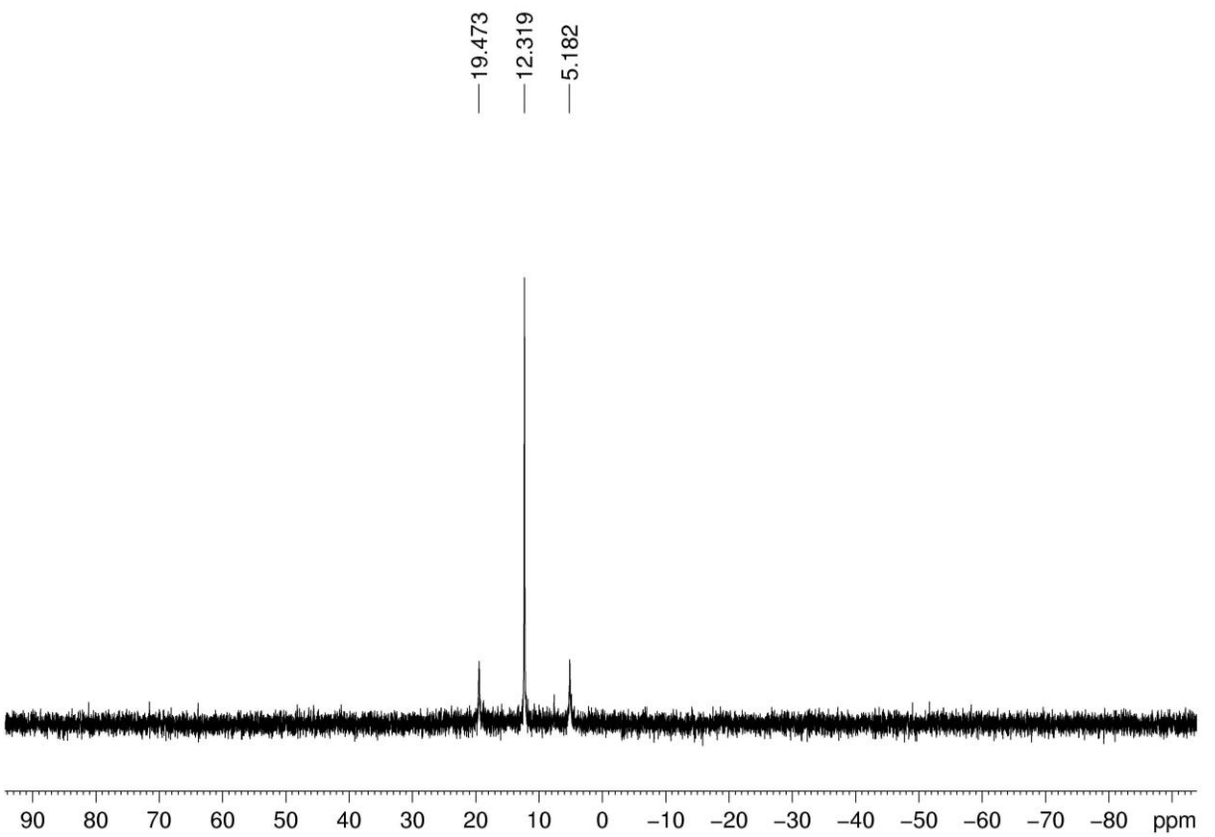

Fig. S2 ^{31}P NMR (162 MHz) spectrum of cis-[Pt_2{$(Ph_2P)_2py$}$_2${$C{\equiv}CC_6H_2(OMe)_3$-3,4,5}$_4$] in d_6-DMSO.

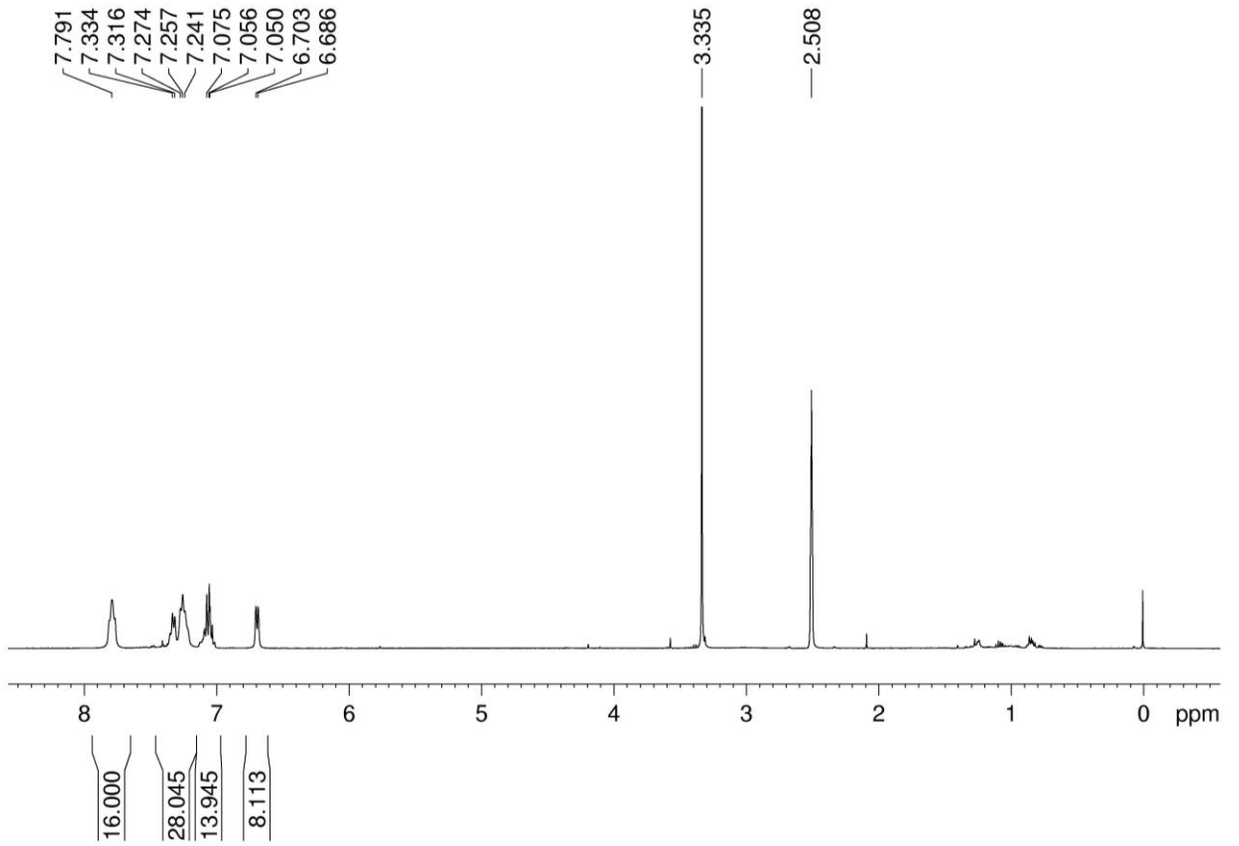

Fig. S3 ^{1}H NMR (400 MHz) spectrum of cis-[Pt_2{$(Ph_2P)_2py$}$_2$($C{\equiv}CC_6H_5$)$_4$] in d_6-DMSO.

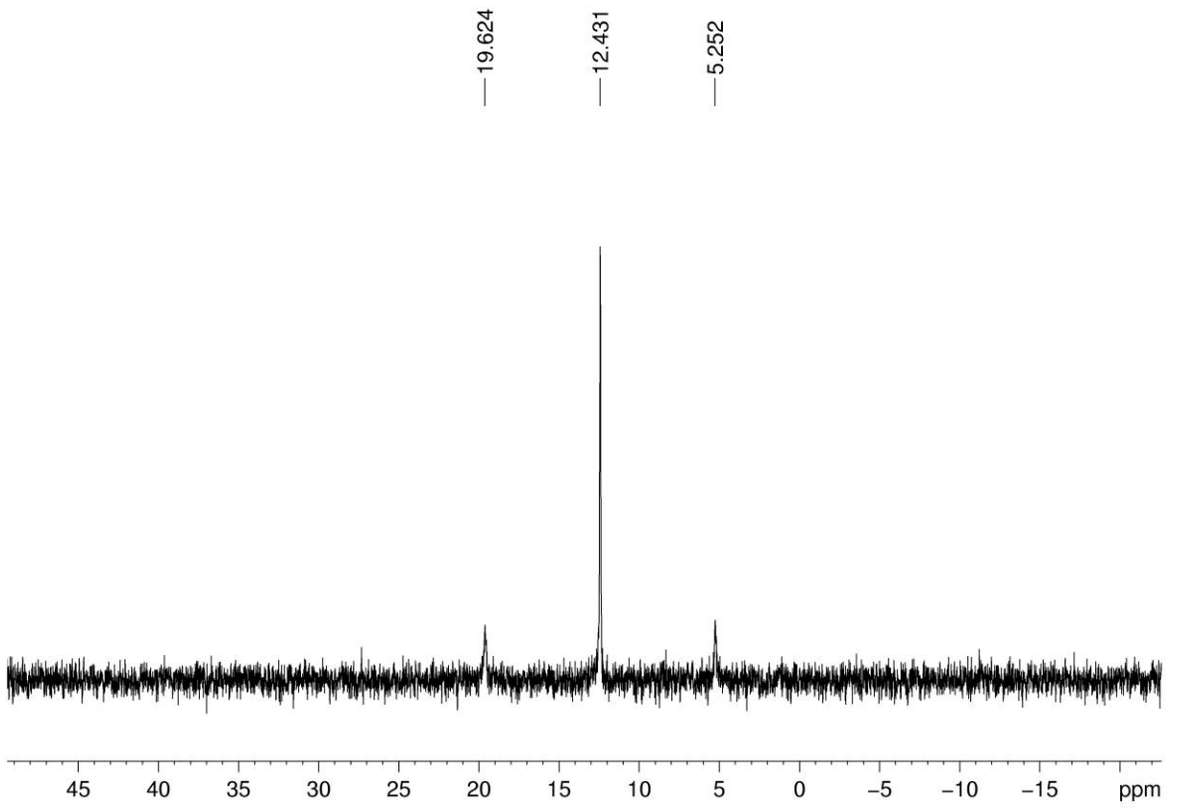

Fig. S4 ^{31}P NMR (162 MHz) spectrum of cis-[Pt_2{$(Ph_2P)_2py$}$_2$($C{\equiv}CC_6H_5$)$_4$] in d_6-DMSO.

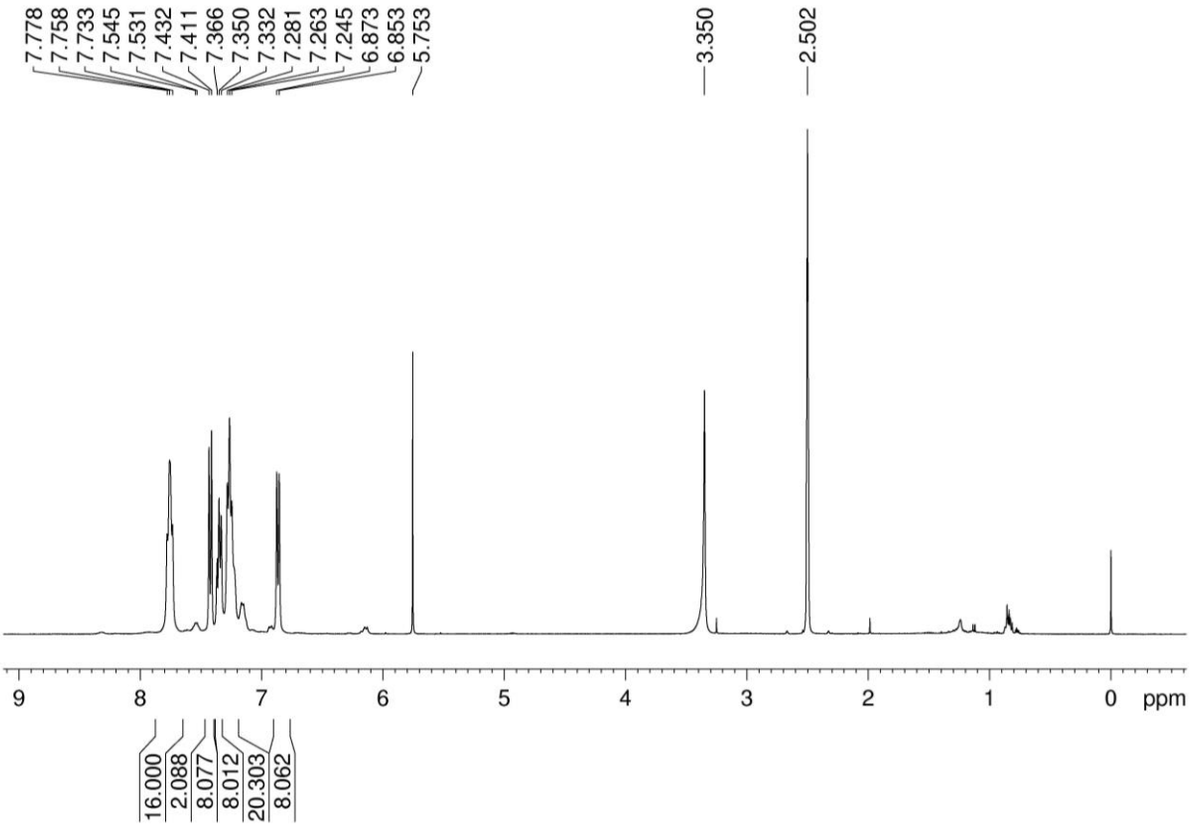

Fig. S5 ^{1}H NMR (400 MHz) spectrum of cis-[Pt_2{$(Ph_2P)_2py$}$_2$($C{\equiv}CC_6H_4CF_3$-4)$_4$] in d_6-DMSO.

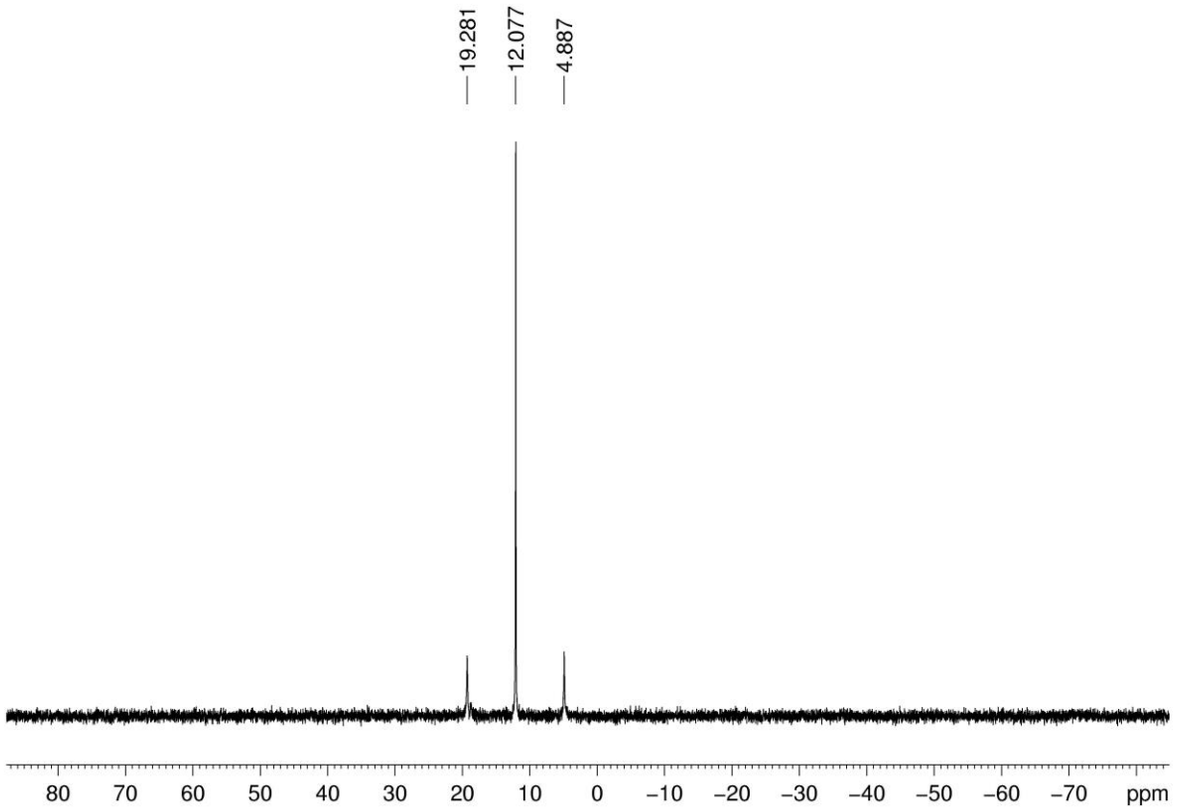

Fig. S6 ^{31}P NMR (162 MHz) spectrum of cis-[Pt_2{$(Ph_2P)_2py$}$_2$($C{\equiv}CC_6H_4CF_3$-4)$_4$] in d_6-DMSO.

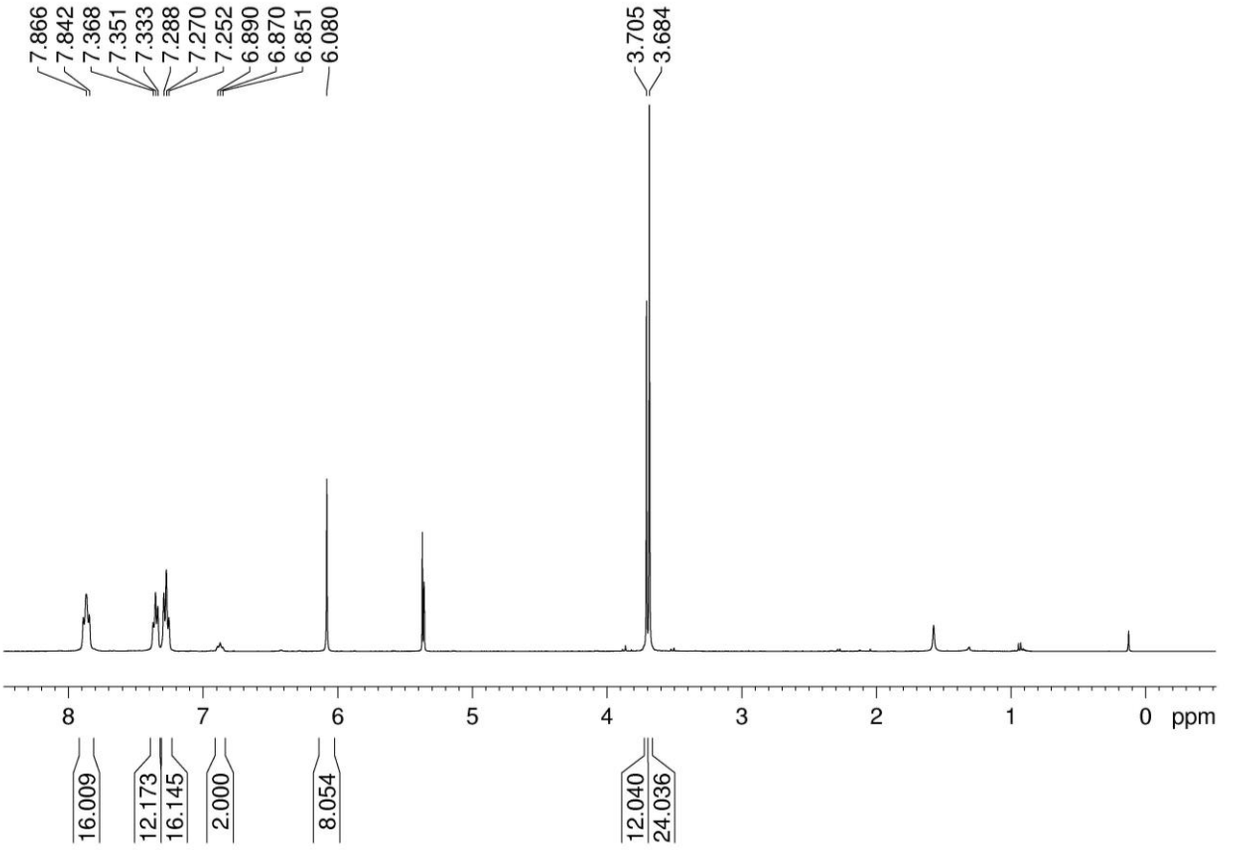

Fig. S7 ^{1}H NMR (400 MHz) spectrum of cis-[Pt_2Ag_2{$(Ph_2P)_2py$}$_2${$C{\equiv}CC_6H_2(OMe)_3$-3,4,5}$_4$]$(SO_3CF_3)_2$ **(1a)** in CD_2Cl_2.

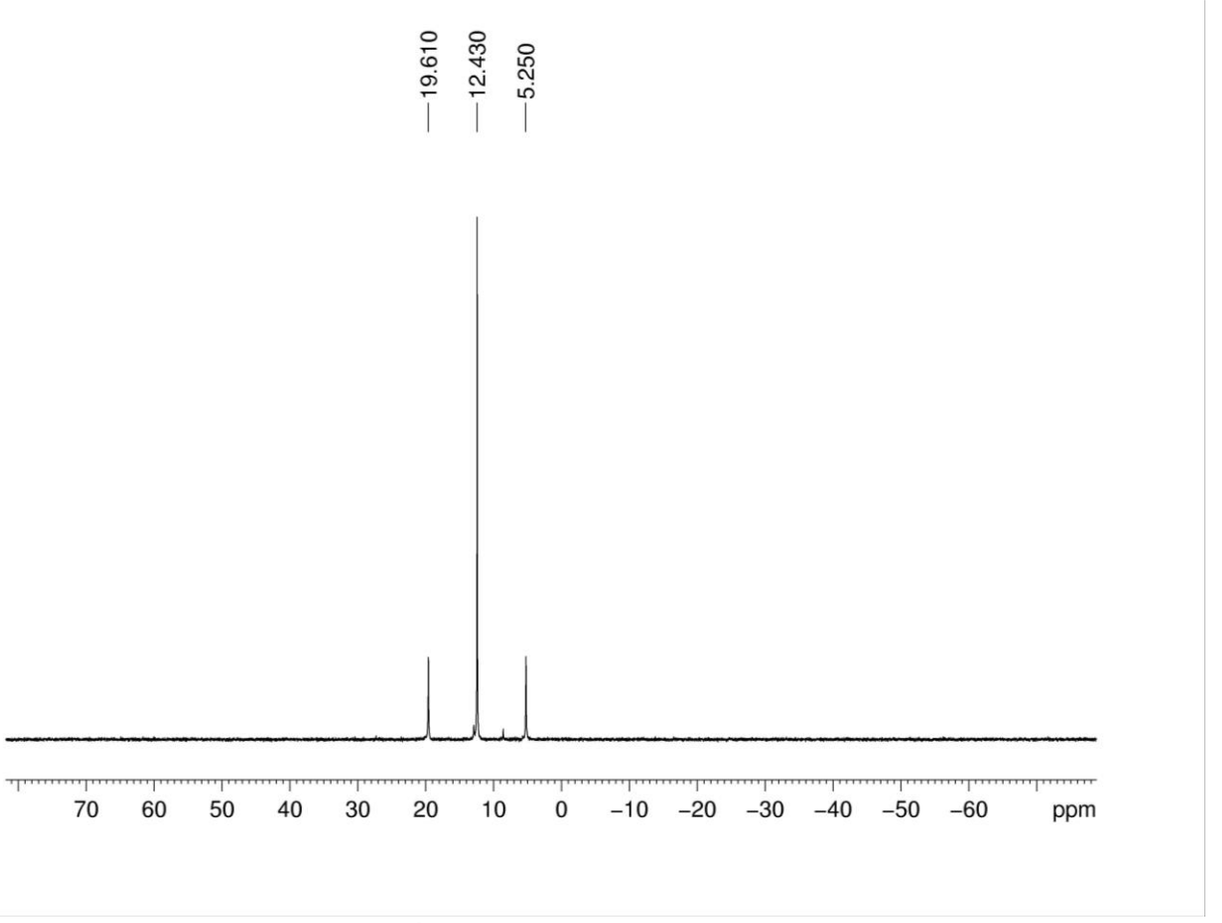

Fig. S8 ^{31}P NMR (162 MHz) spectrum of cis-[Pt_2Ag_2{$(Ph_2P)_2py$}$_2${$C{\equiv}CC_6H_2(OMe)_3$-3,4,5}$_4$]$(SO_3CF_3)_2$ **(1a)** in CD_2Cl_2.

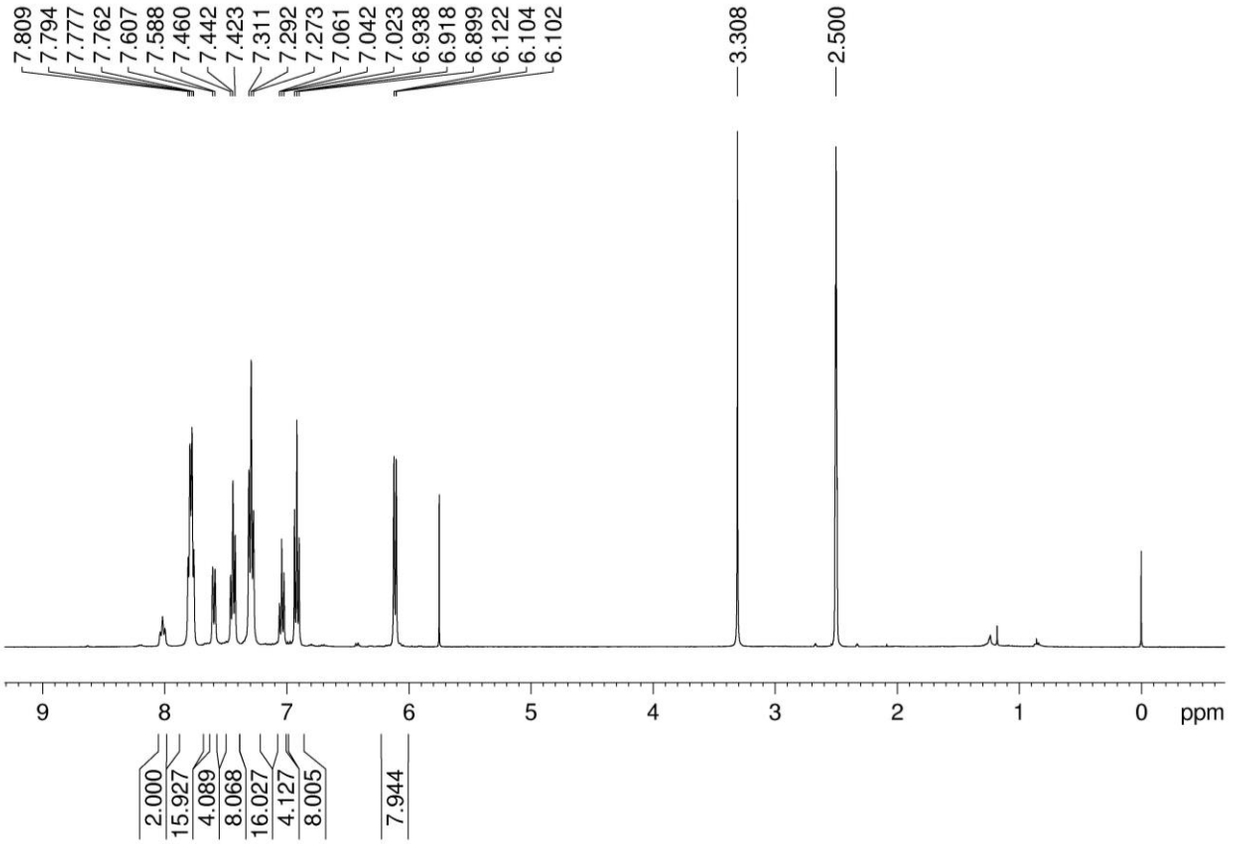

Fig. S9 ^{1}H NMR (400 MHz) spectrum of cis-[Pt_2Ag_2{$(Ph_2P)_2py$}$_2$($C{\equiv}CC_6H_5$)$_4$](SO_3CF_3)$_2$ **(2a)** in d_6-DMSO.

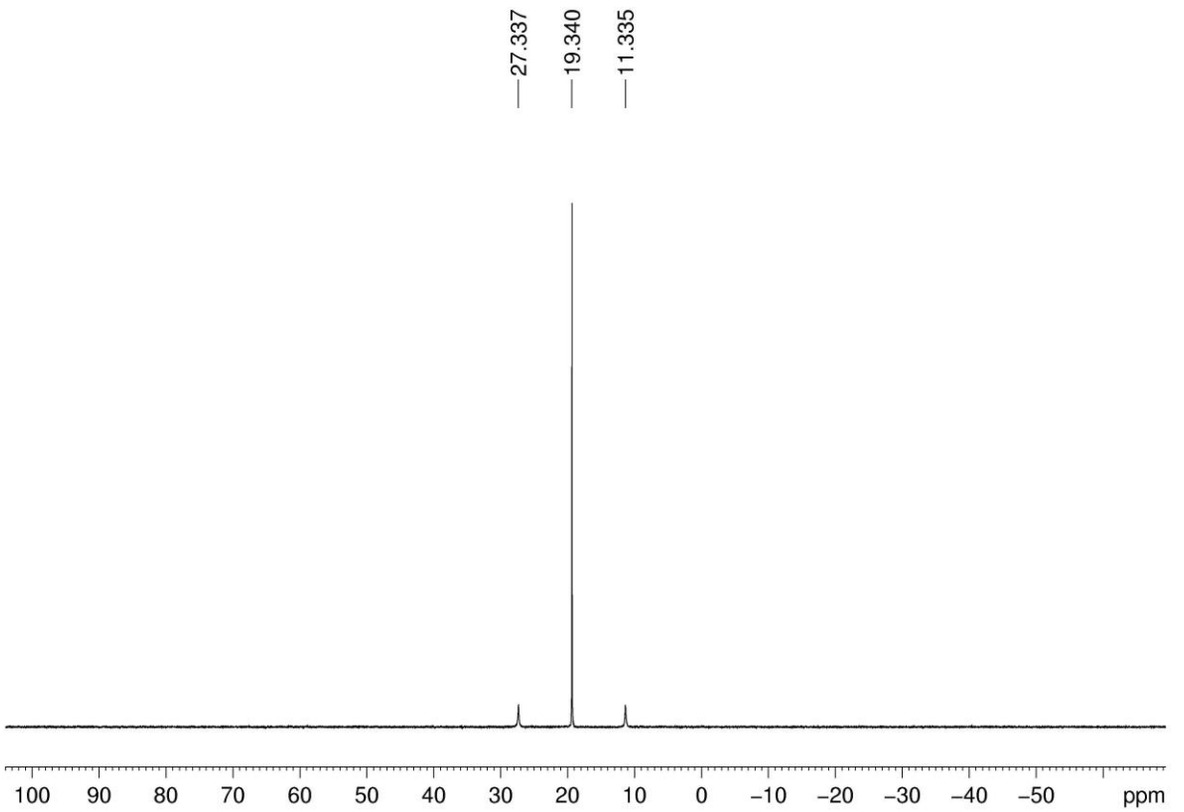

Fig. S10 ^{31}P NMR (162 MHz) spectrum of cis-[Pt_2Ag_2{$(Ph_2P)_2py$}$_2$($C{\equiv}CC_6H_5$)$_4$](SO_3CF_3)$_2$ **(2a)** in d_6-DMSO.

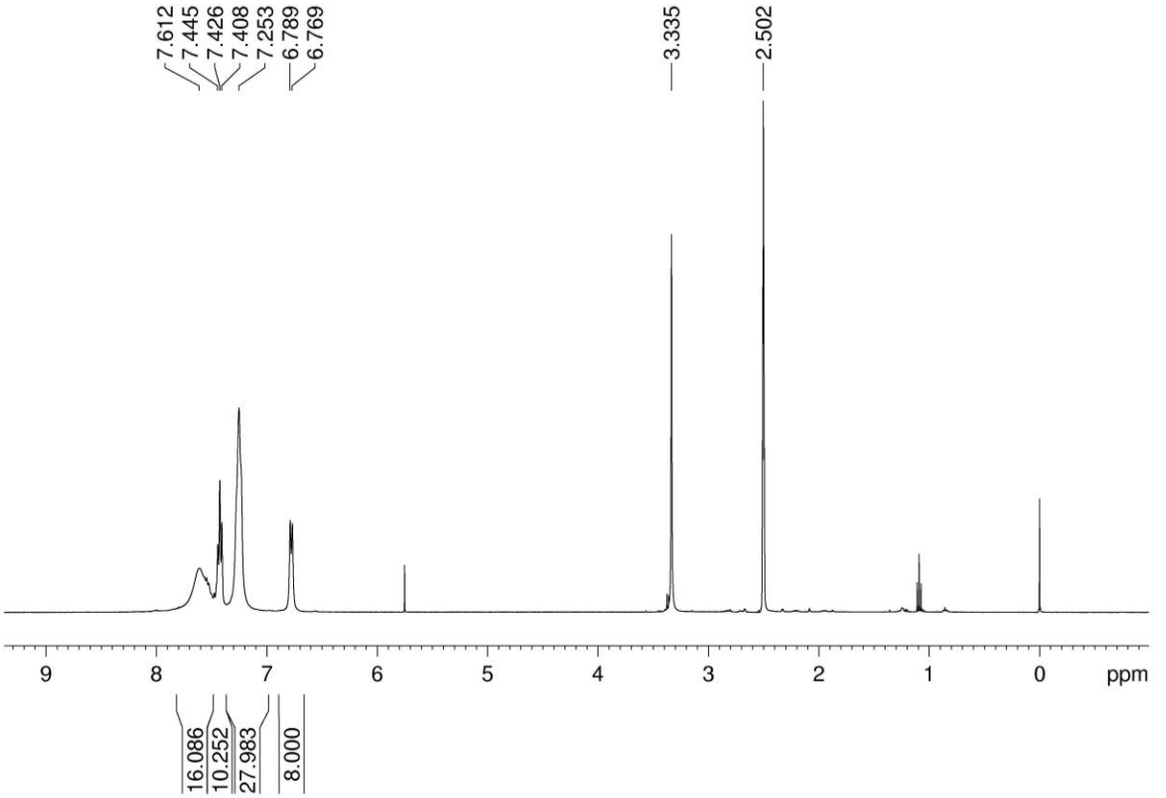

Fig. S11 ^{1}H NMR (400 MHz) spectrum of cis-[Pt_2Ag_2{$(Ph_2P)_2py$}$_2$($C{\equiv}CC_6H_4CF_3$-4)$_4$](SO_3CF_3)$_2$ **(3a)** in d_6-DMSO.

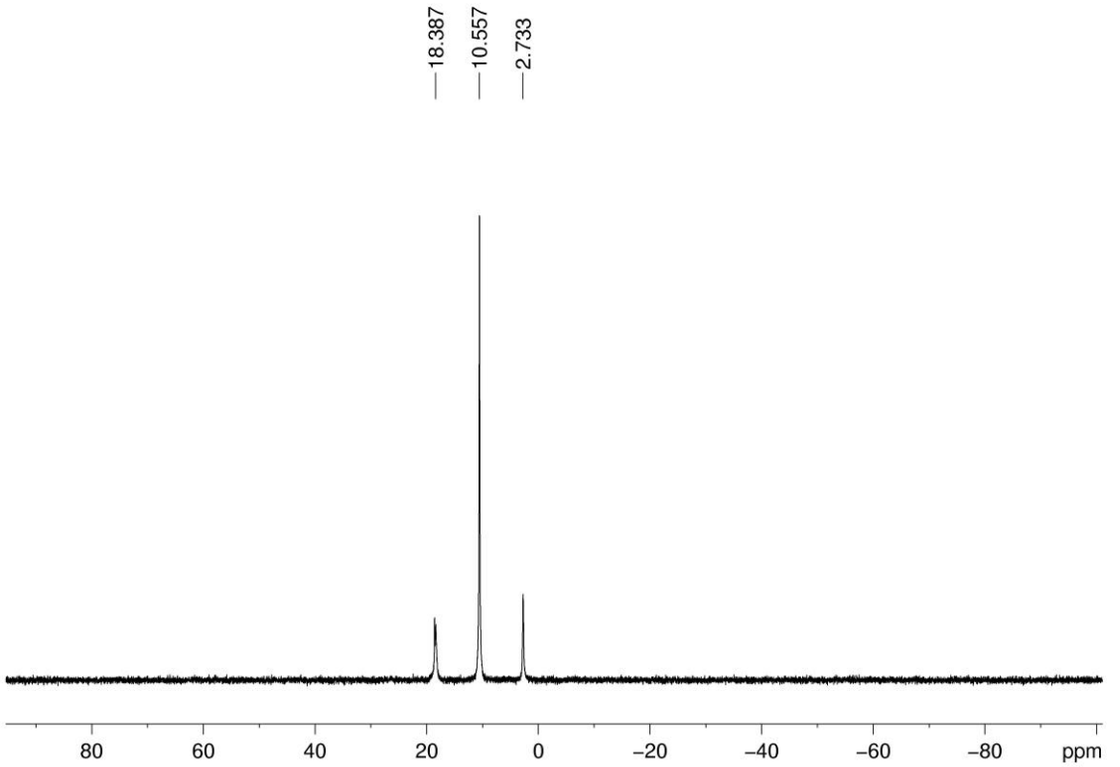

Fig. S12 ^{31}P NMR (162 MHz) spectrum of cis-[Pt_2Ag_2{$(Ph_2P)_2py$}$_2$($C{\equiv}CC_6H_4CF_3$-4)$_4$](SO_3CF_3)$_2$ **(3a)** in d_6-DMSO.

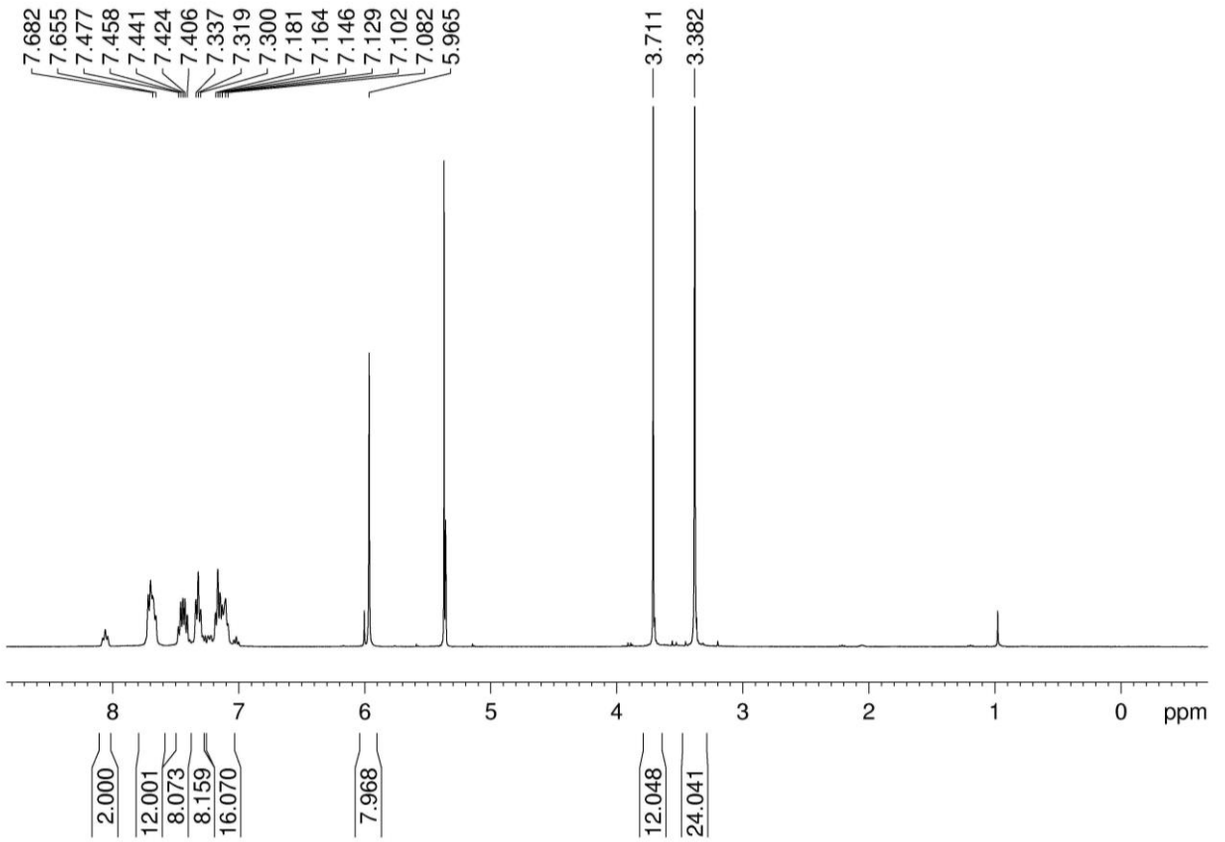

Fig. S13 ^{1}H NMR (400 MHz) spectrum of trans-[Pt_2Ag_2{$(Ph_2P)_2py$}$_2$($C{\equiv}CC_6H_2(OMe)_3$-3,4,5)$_4$]$(SO_3CF_3)_2$ **(1b)** in CD_2Cl_2.

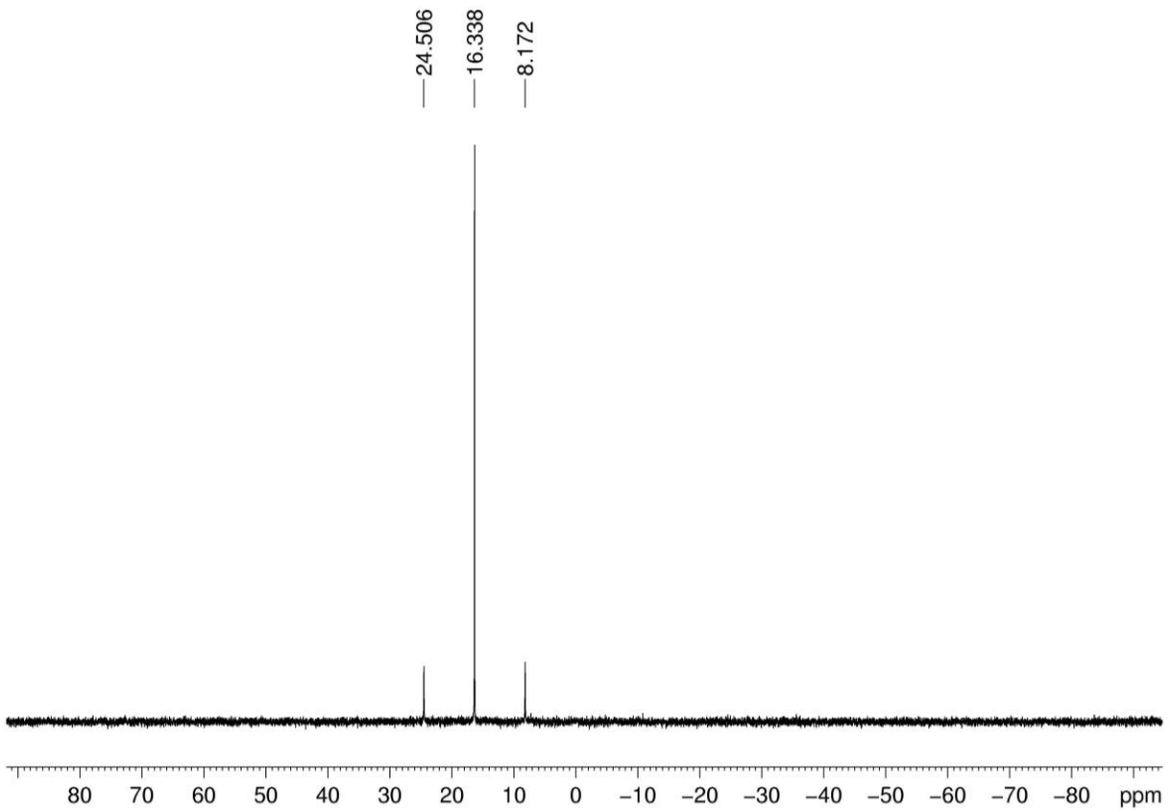

Fig. S14 ^{31}P NMR (162 MHz) spectrum of trans-[Pt_2Ag_2{$(Ph_2P)_2py$}$_2$($C{\equiv}CC_6H_2(OMe)_3$-3,4,5)$_4$]$(SO_3CF_3)_2$ **(1b)** in CD_2Cl_2.

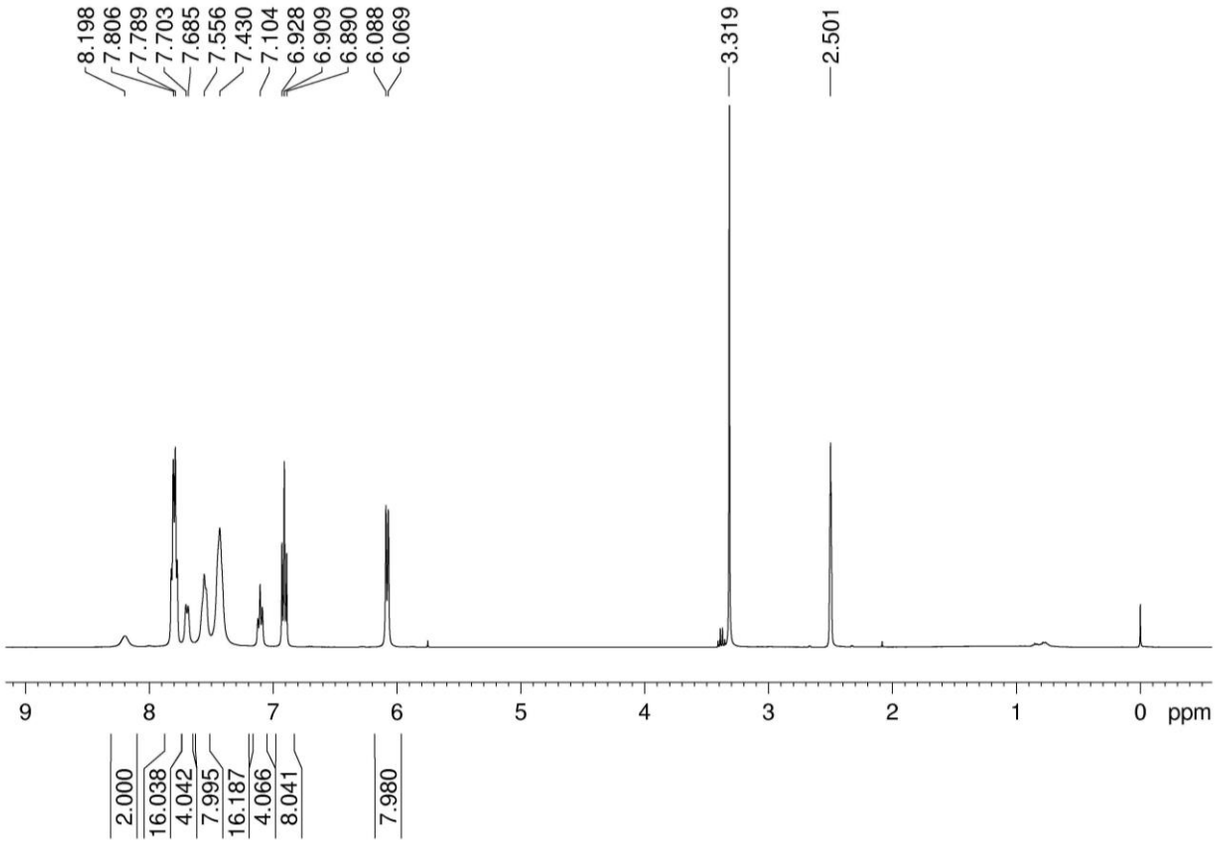

Fig. S15 ^{1}H NMR (400 MHz) spectrum of trans-[$Pt_2Ag_2\{(Ph_2P)_2py\}_2(C{\equiv}CC_6H_5)_4](SO_3CF_3)_2$ **(2b)** in d_6-DMSO.

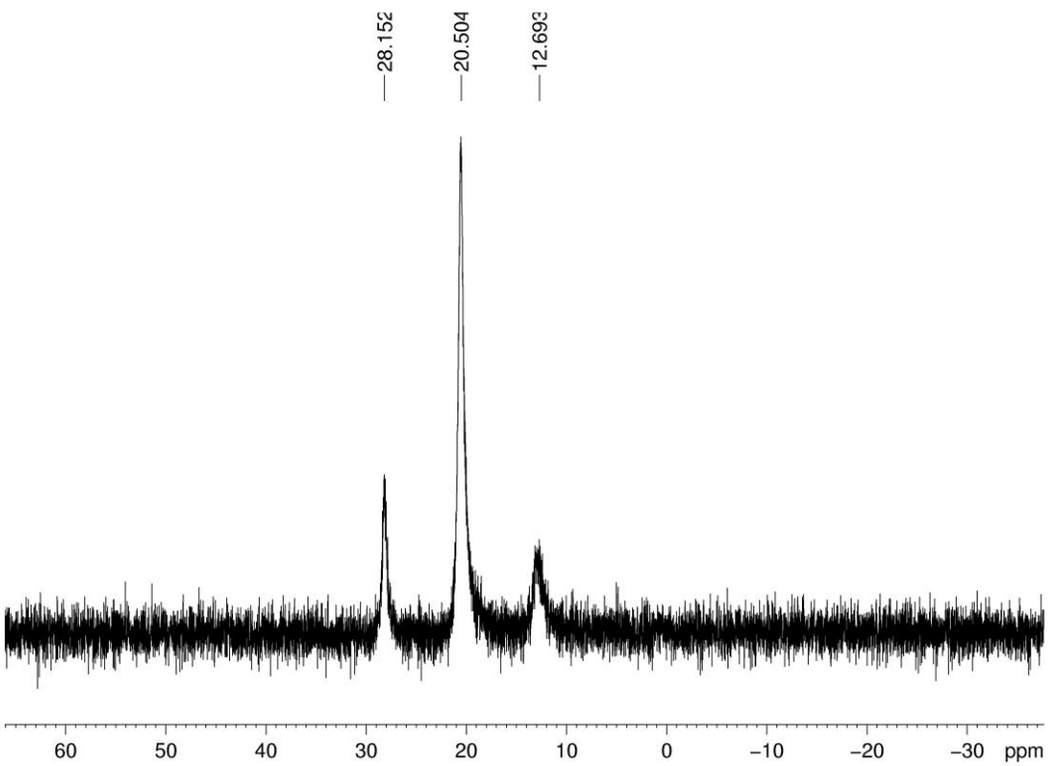

Fig. S16 ^{31}P NMR (162 MHz) spectrum of trans-[$Pt_2Ag_2\{(Ph_2P)_2py\}_2(C{\equiv}CC_6H_5)_4](SO_3CF_3)_2$ **(2b)** in d_6-DMSO.

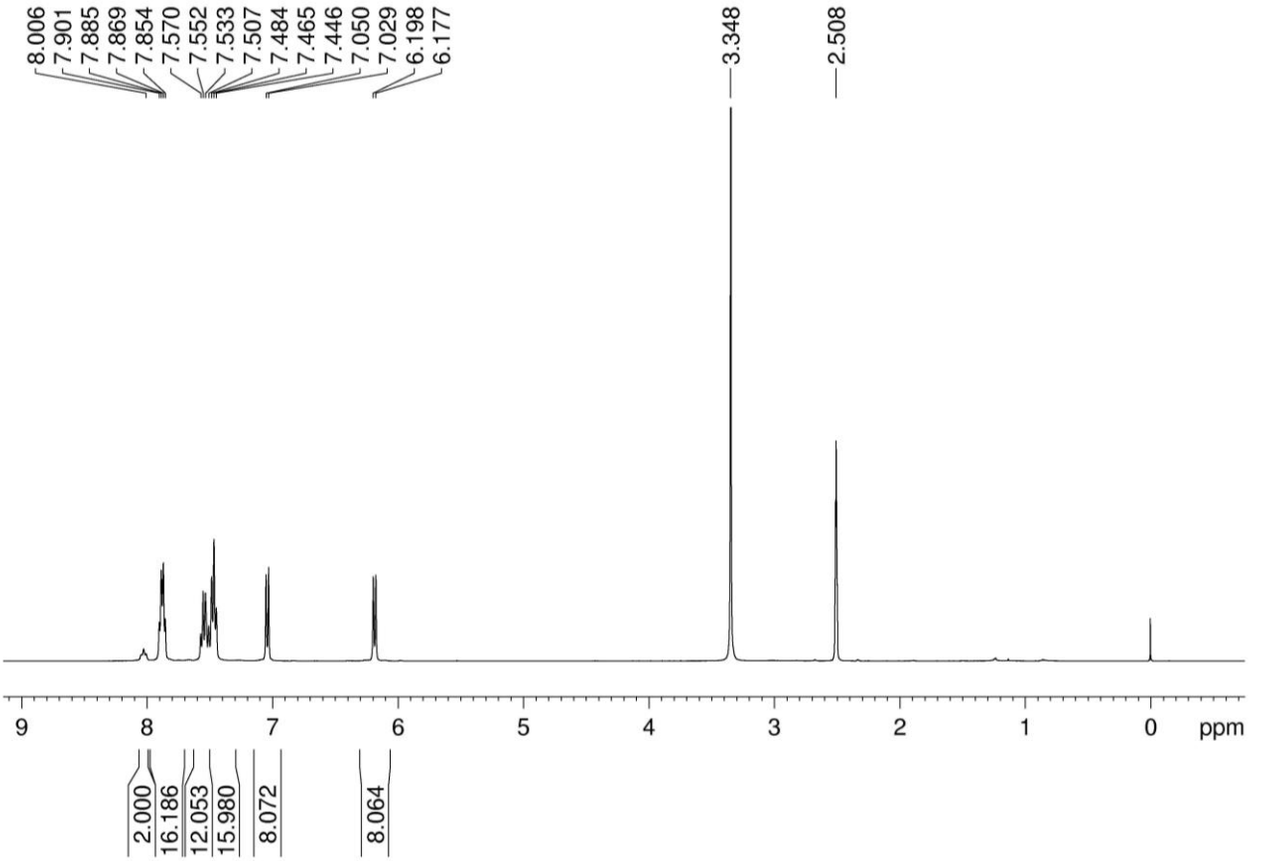

Fig. S17 ^{1}H NMR (400 MHz) spectrum of trans-[Pt_2Ag_2{$(Ph_2P)_2py$}$_2$($C{\equiv}CC_6H_4CF_3$-4)$_4$](SO_3CF_3)$_2$ **(3b)** in d_6-DMSO.

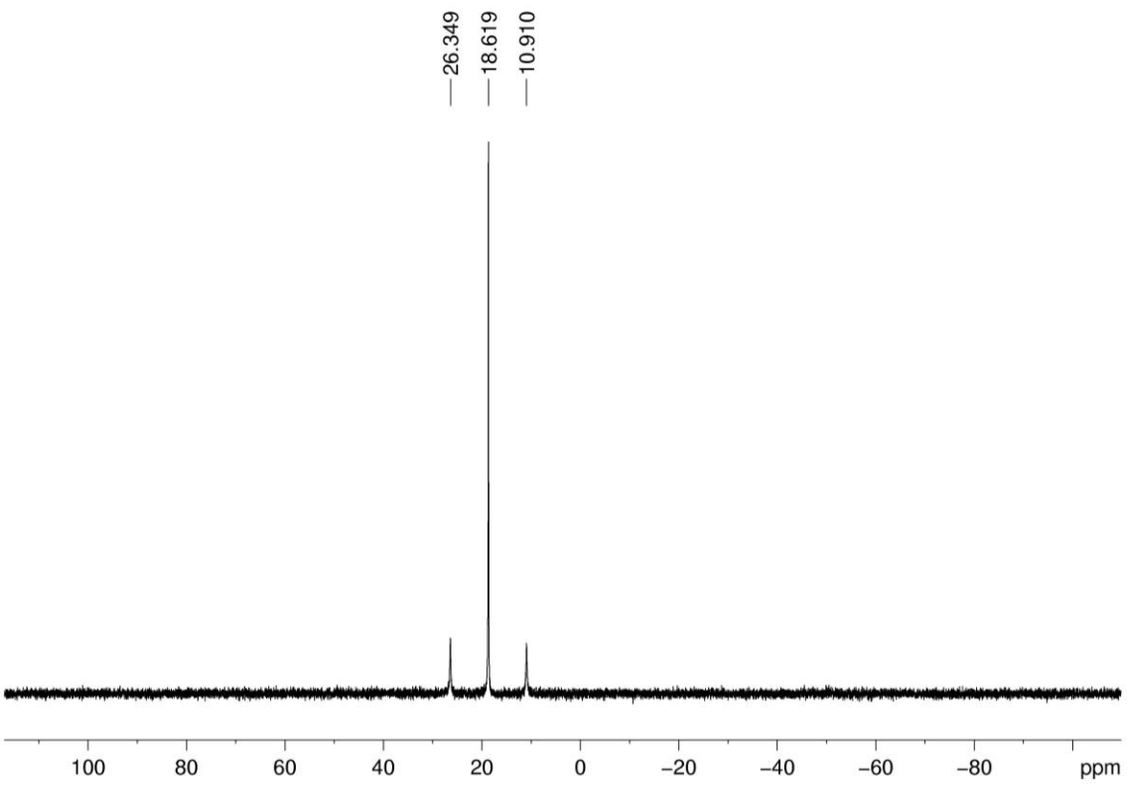

Fig. S18 ^{31}P NMR (162 MHz) spectrum of trans-[Pt_2Ag_2{$(Ph_2P)_2py$}$_2$($C{\equiv}CC_6H_4CF_3$-4)$_4$](SO_3CF_3)$_2$ **(3b)** in d_6-DMSO.

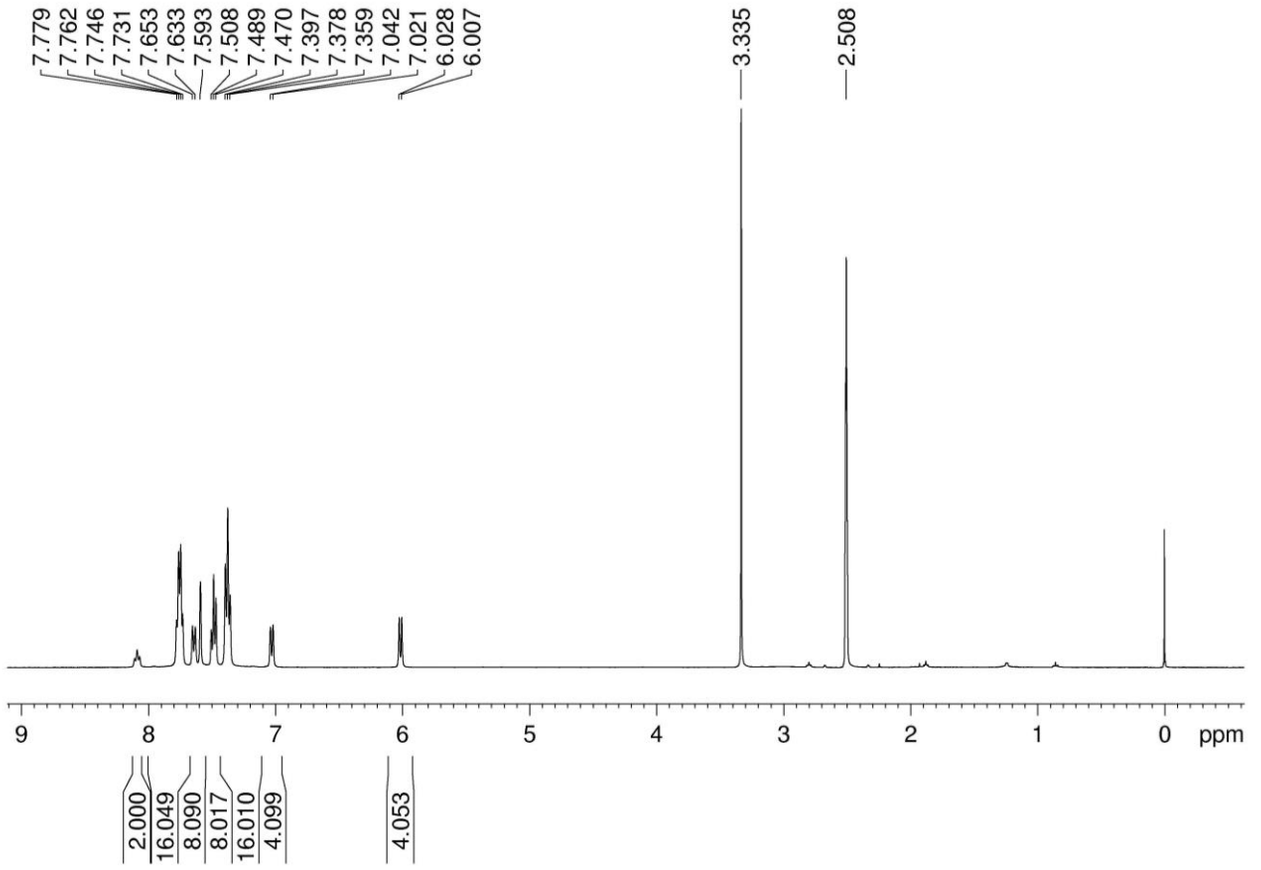

Fig. S19 ^{1}H NMR (400 MHz) spectrum of trans-[Pt_2Ag_2{$(Ph_2P)_2py$}$_2$($C{\equiv}CC_6H_3(CF_3)_2$-2,4}$_4$]$(SO_3CF_3)_2$ **(4b)** in d_6-DMSO.

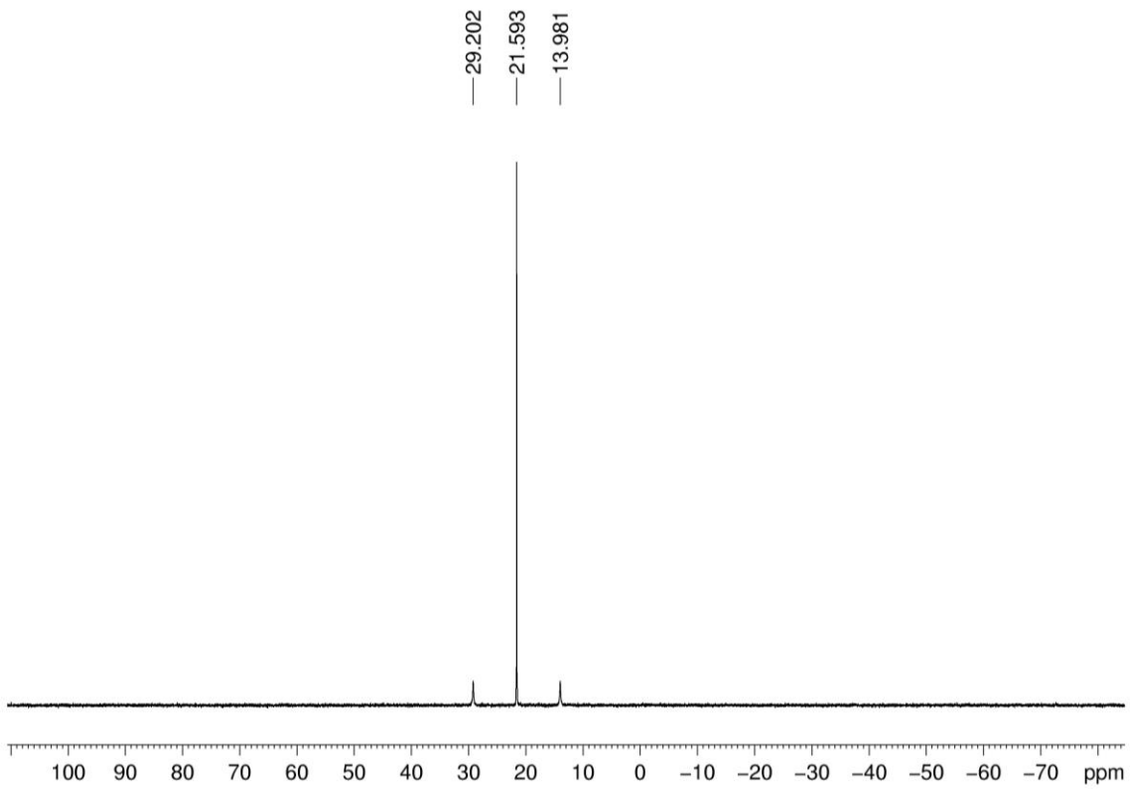

Fig. S20 ^{31}P NMR (162 MHz) spectrum of trans-[Pt_2Ag_2{$(Ph_2P)_2py$}$_2$($C{\equiv}CC_6H_3(CF_3)_2$-2,4}$_4$]$(SO_3CF_3)_2$ **(4b)** in d_6-DMSO.

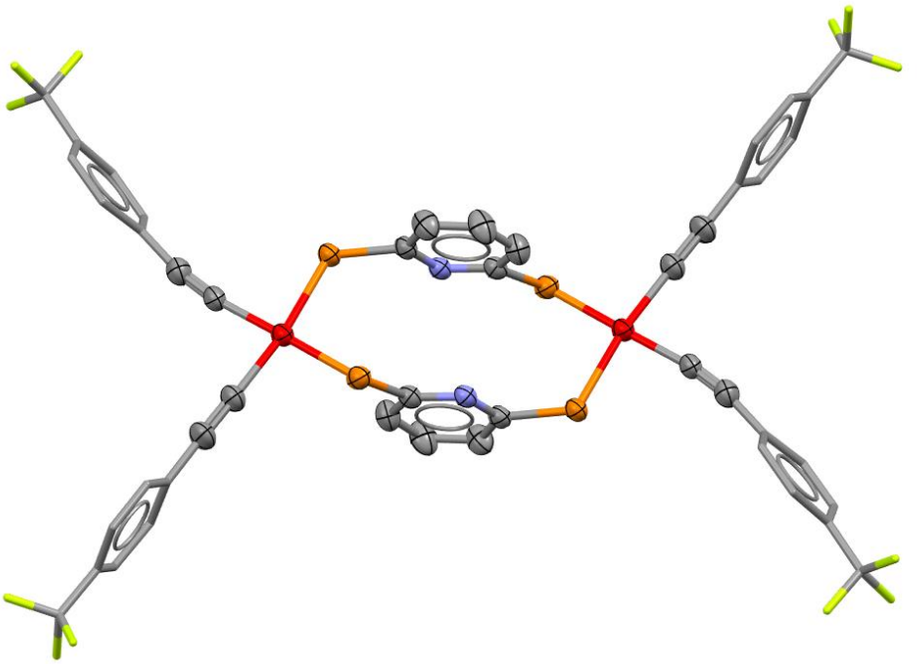

Fig. S21 Perspective view (30% thermal ellipsoids) of cis-binuclear complex cis-$Pt_2\{(Ph_2P)_2py\}_2(C{\equiv}CC_6H_4CF_4\text{-}4)_4$. The 4-trifluoromethyl-1-phenyl rings were depicted without using thermal ellipsoids. Phenyl rings on the phosphorus atoms are omitted for clarity.

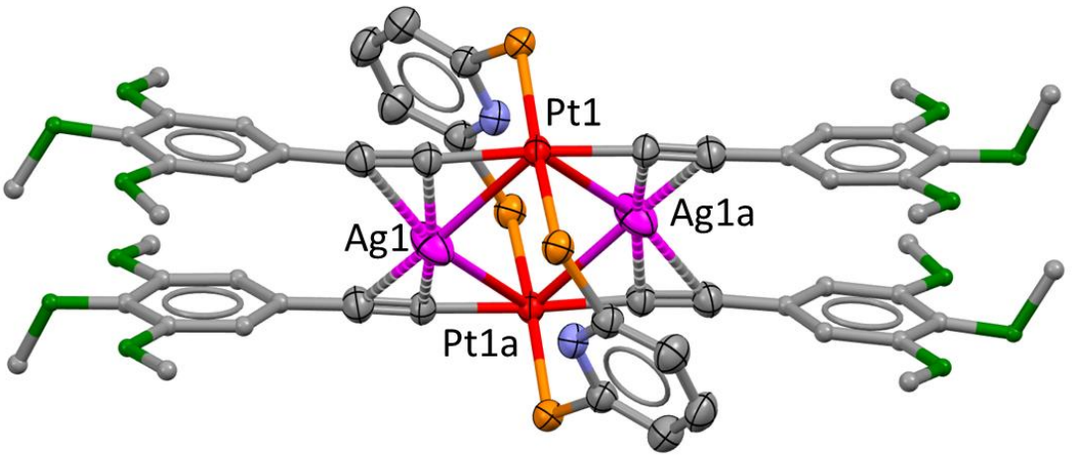

Fig. S22 Perspective view (30% thermal ellipsoids) of trans-Pt_2Ag_2 complex **1b**. The 3,4,5-trimethoxy-1-phenyl rings were depicted without using thermal ellipsoids. Phenyl rings on the phosphorus atoms are omitted for clarity.

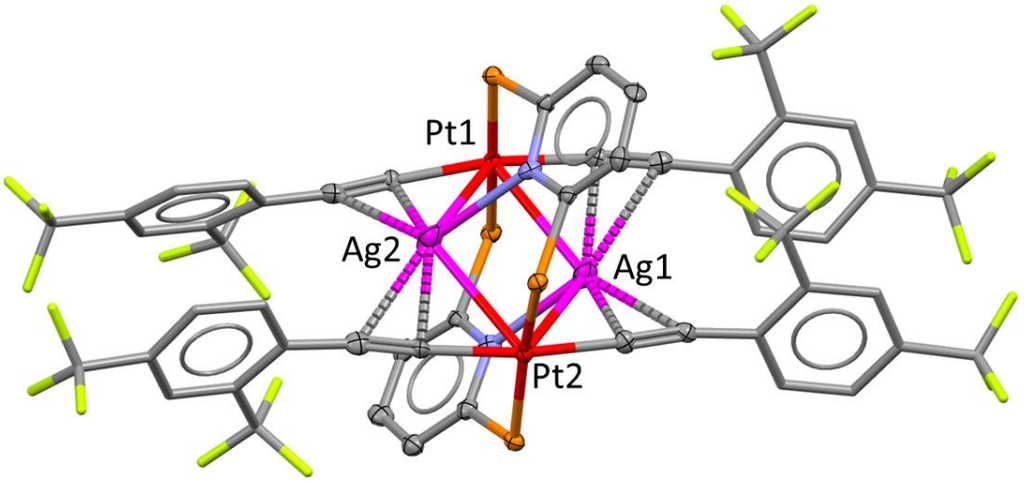

Fig. S23 Perspective view (30% thermal ellipsoids) of trans-Pt_2Ag_2 complex **4b**. The 2,4-bis (trifluoromethyl)-1-phenyl rings were depicted without using thermal ellipsoids. Phenyl rings on the phosphorus atoms are omitted for clarity.

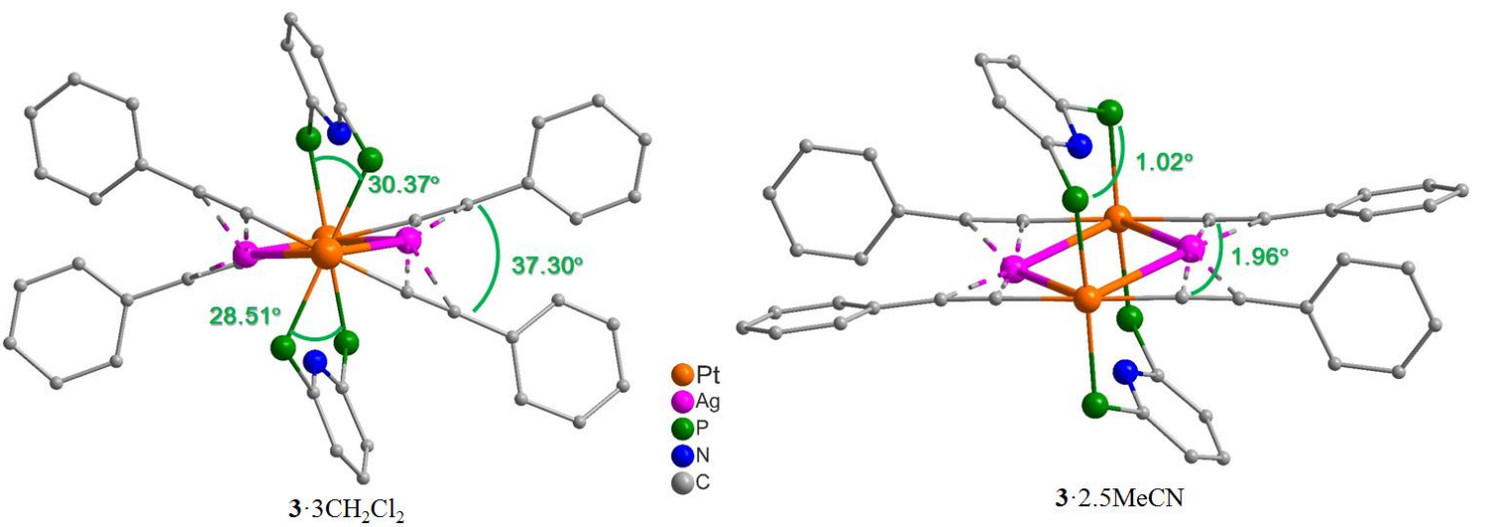

Fig. S24 Dihedral angles in crystal structures of **2b**·$3CH_2Cl_2$ (left) and **2b**·2.5MeCN (right).

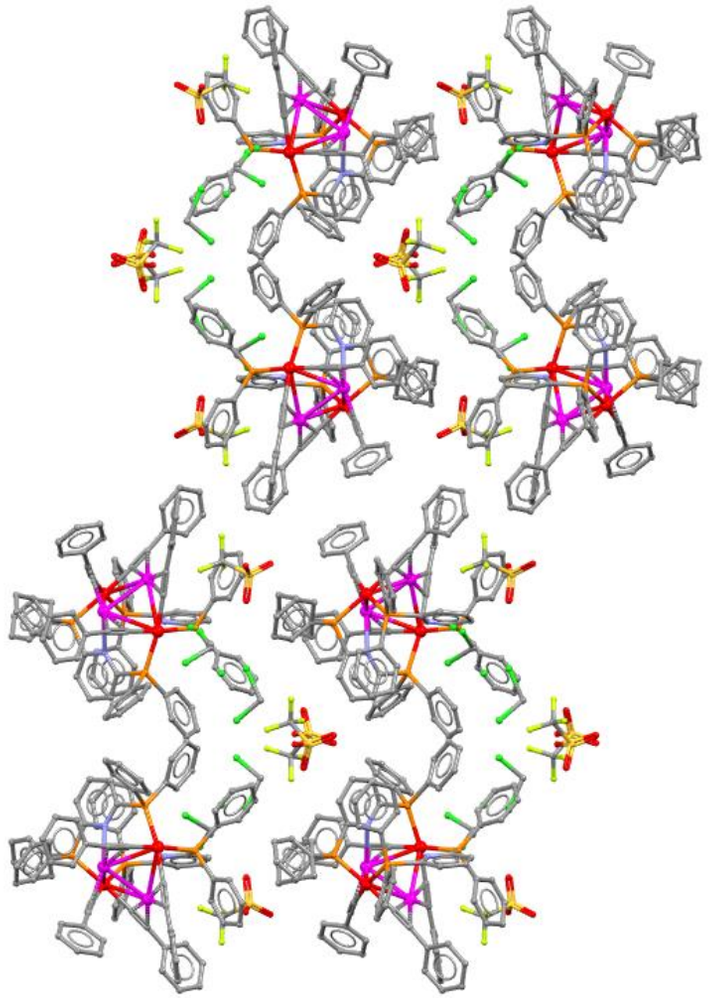

Fig. S25 A view of crystal packing of **2a**·11/4CH_2Cl_2 along a-axis.

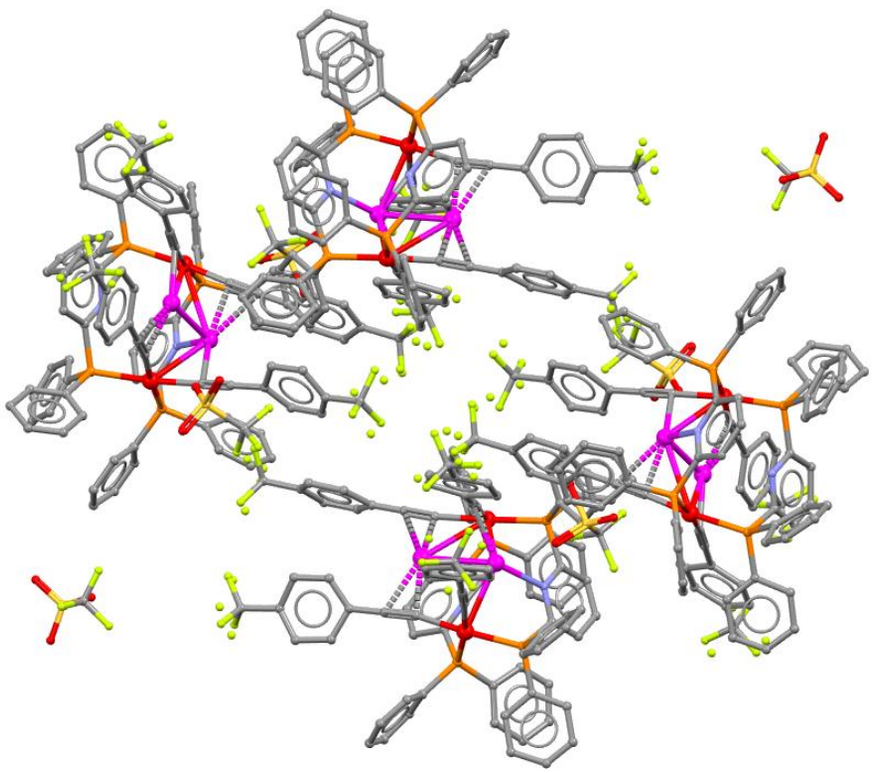

Fig. S26 A view of crystal packing of **3a**·5/2CH_2Cl_2 along b-axis.

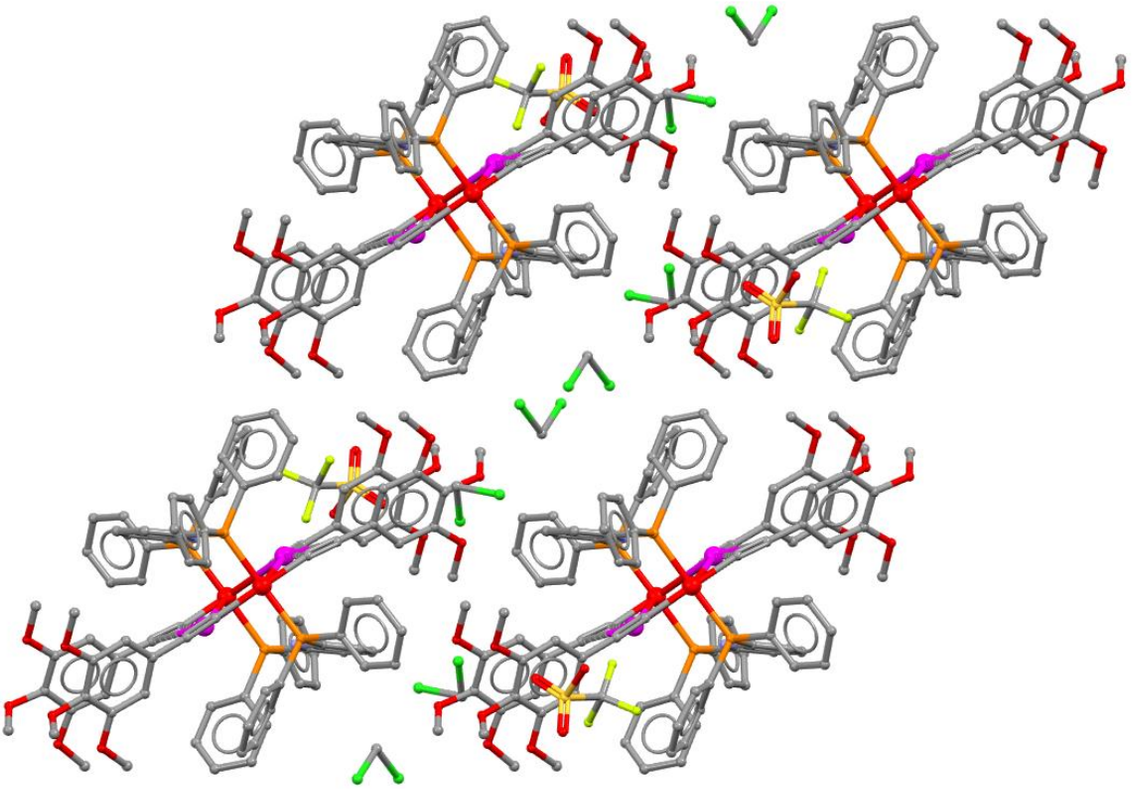

Fig. S27 A view of crystal packing of **1b**·4CH_2Cl_2 along a-axis.

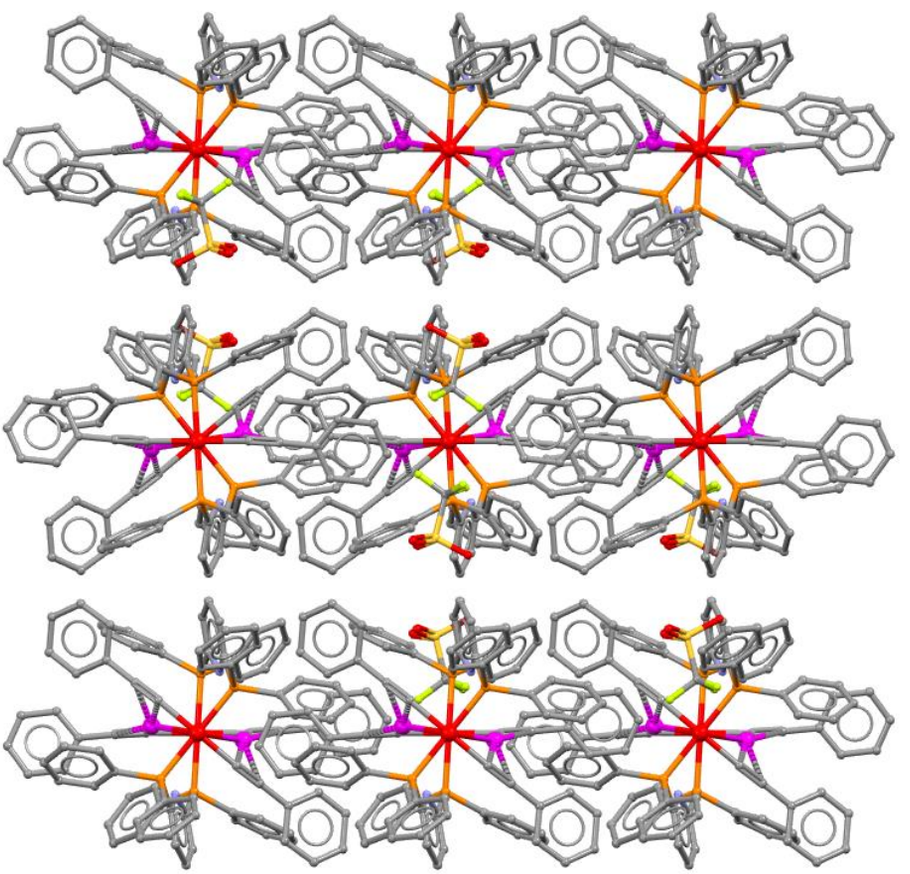

Fig. S28 A view of crystal packing of **2b** along a-axis.

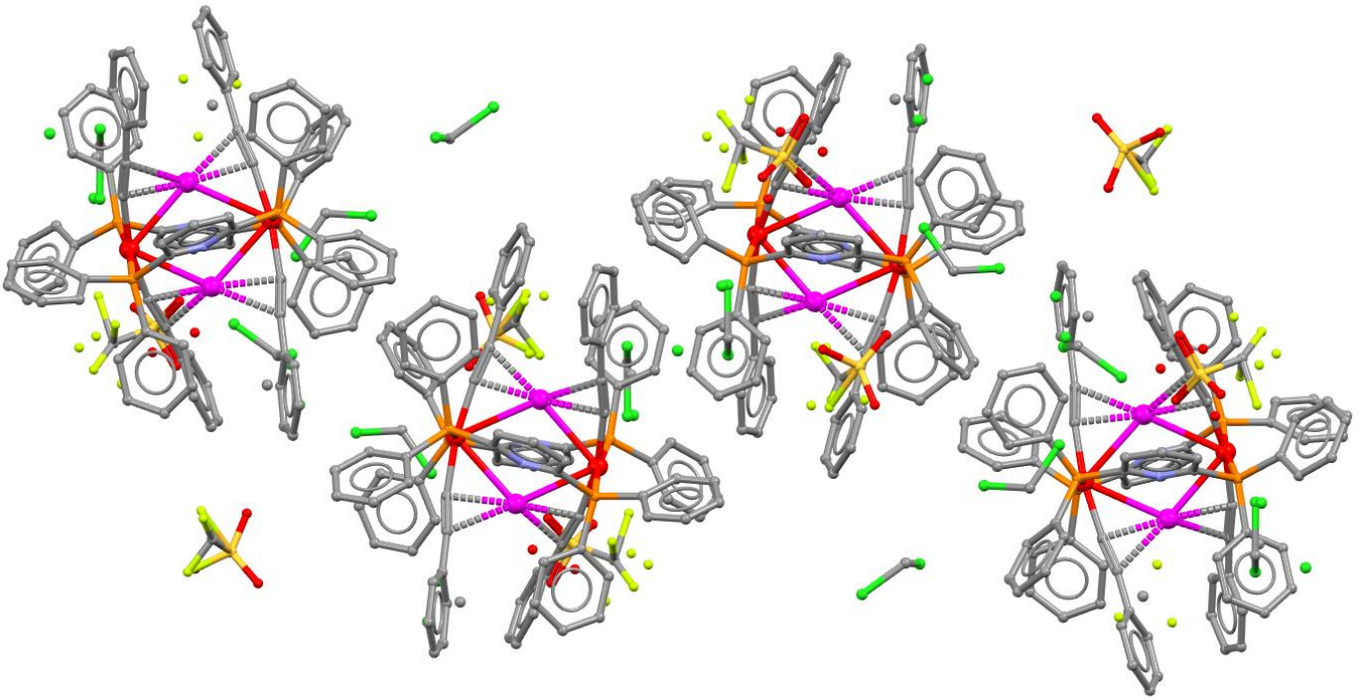

Fig. S29. A view of crystal packing of **2b**·3CH_2Cl_2 along a-axis.

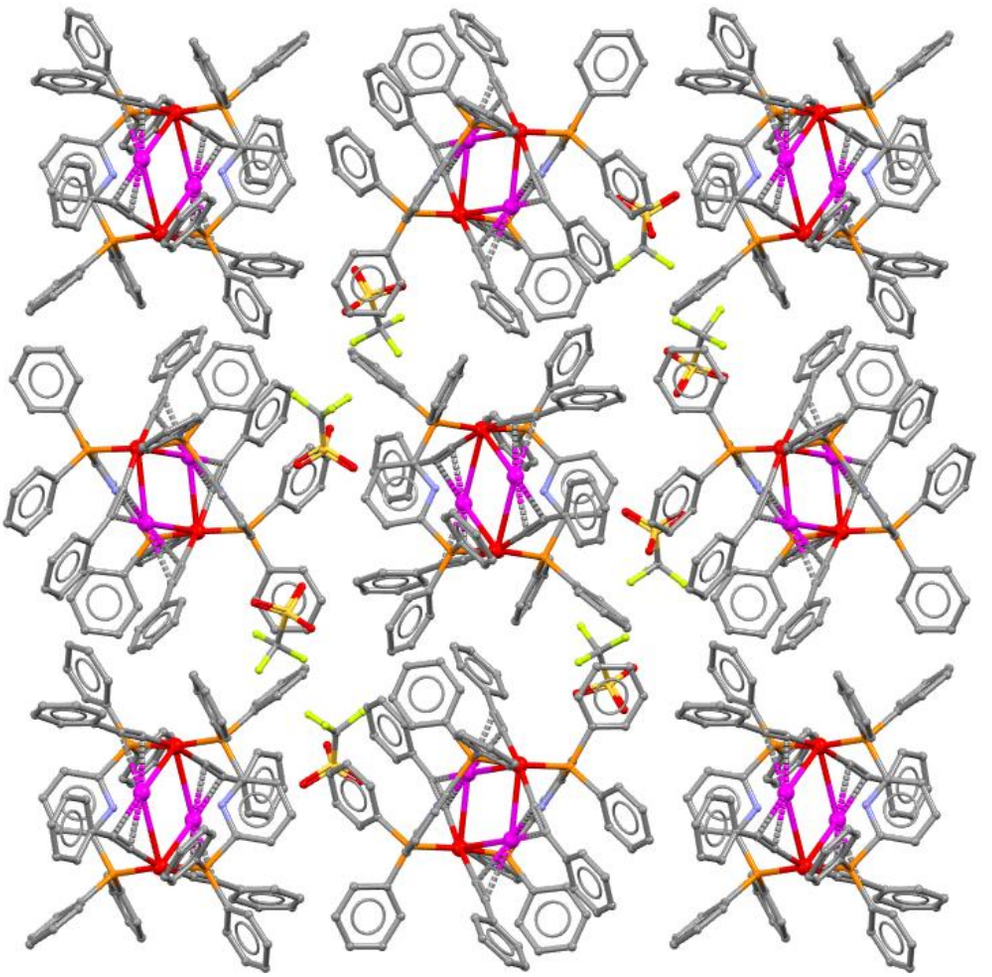

Fig. S30. A view of crystal packing of **2b**·2.5MeCN along a-axis.

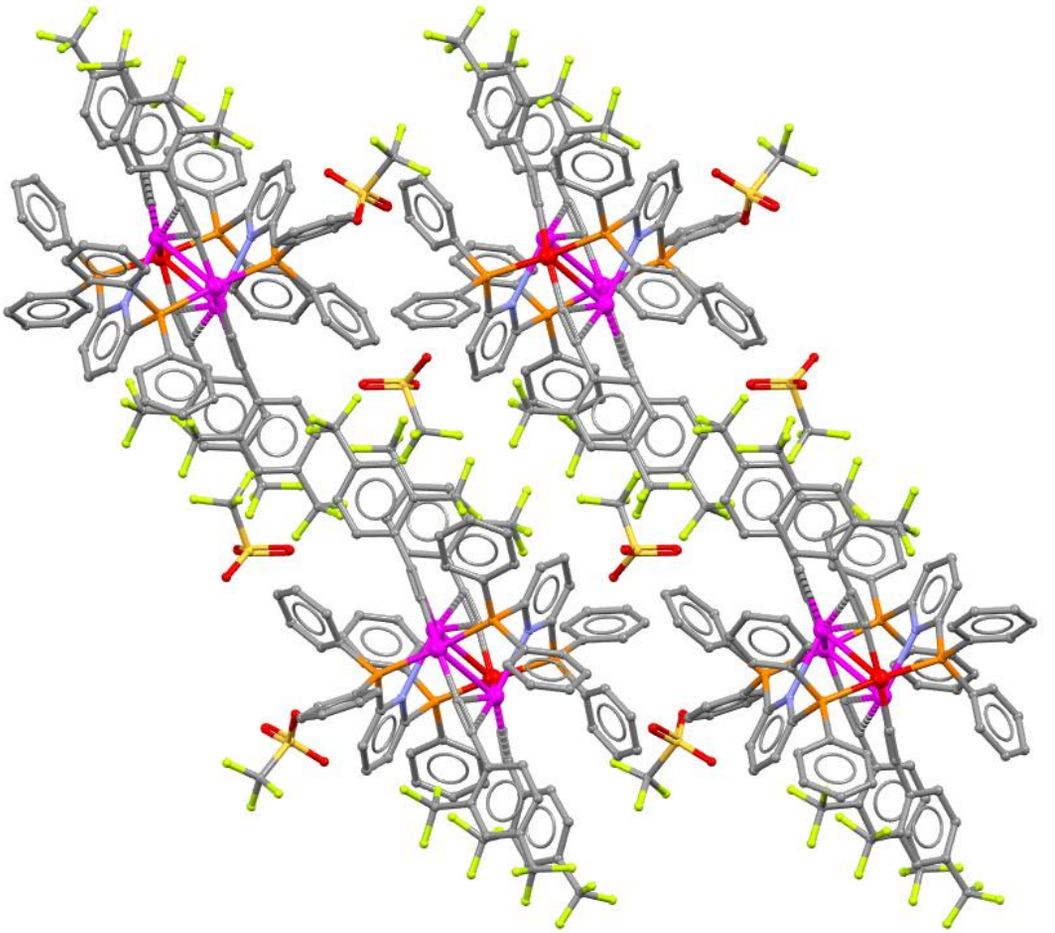

Fig. S31. A view of crystal packing of **4b** along b-axis.

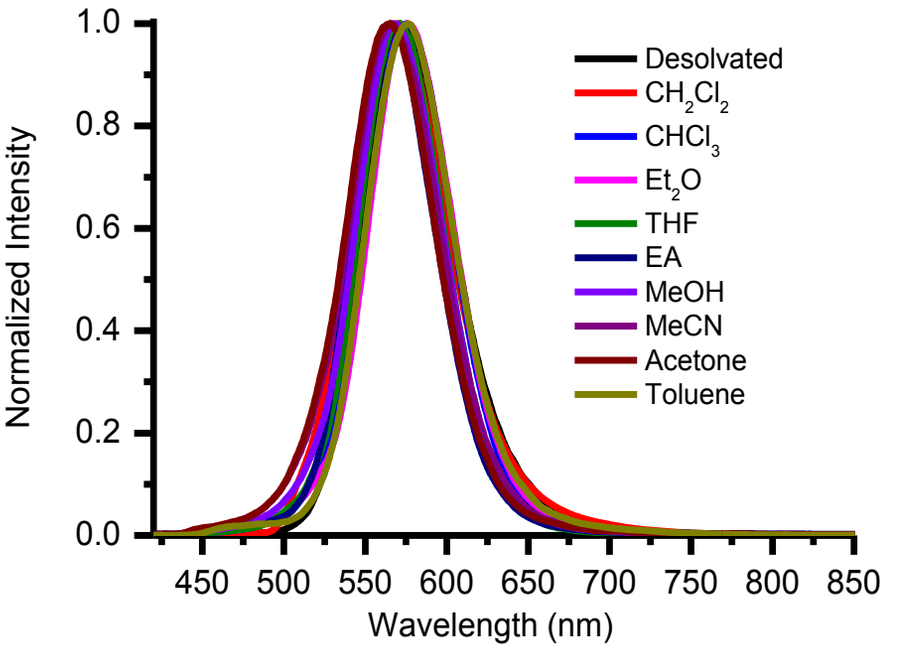

Fig. S32 Emission spectra of solid-state **1b** with various vapours at ambient temperature.

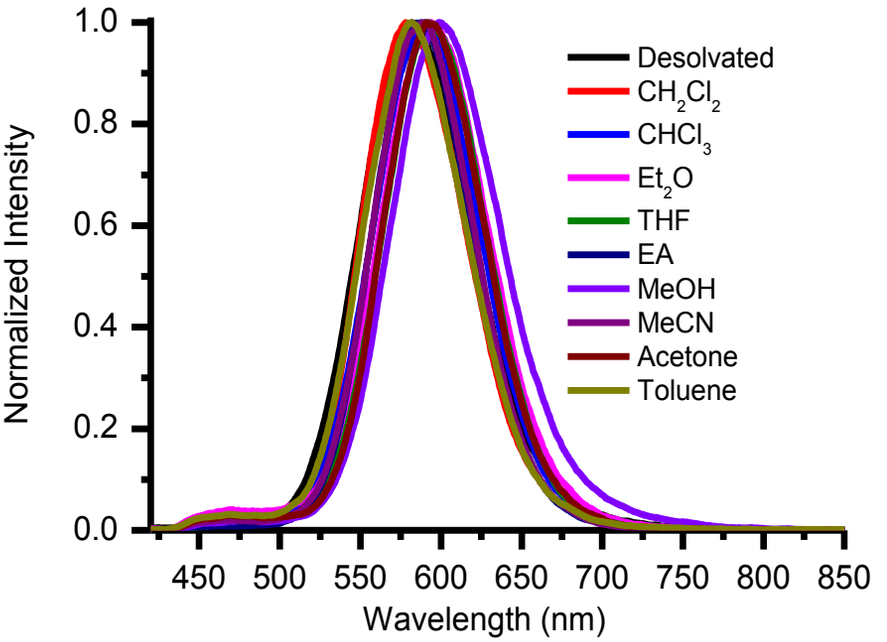

Fig. S33 Emission spectra of solid-state **3b** with various vapours at ambient temperature.

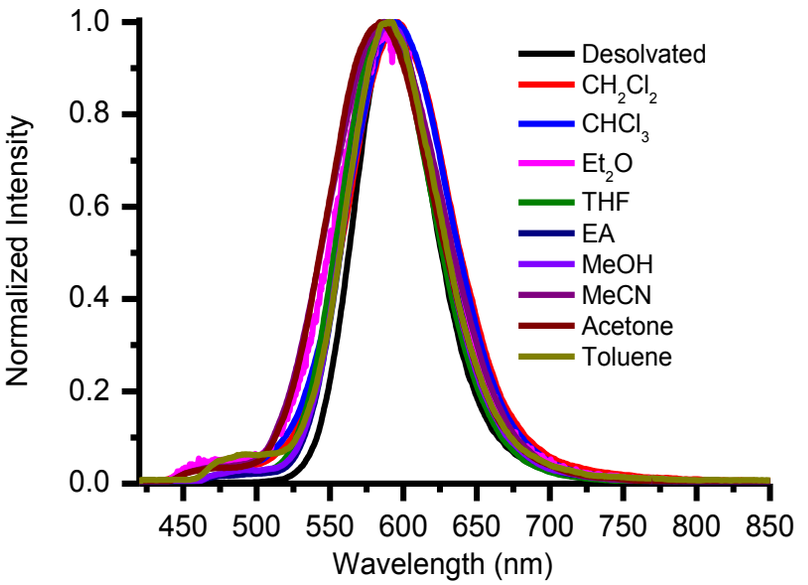

Fig. S34 Emission spectra of solid-state **4b** with various vapours at ambient temperature.

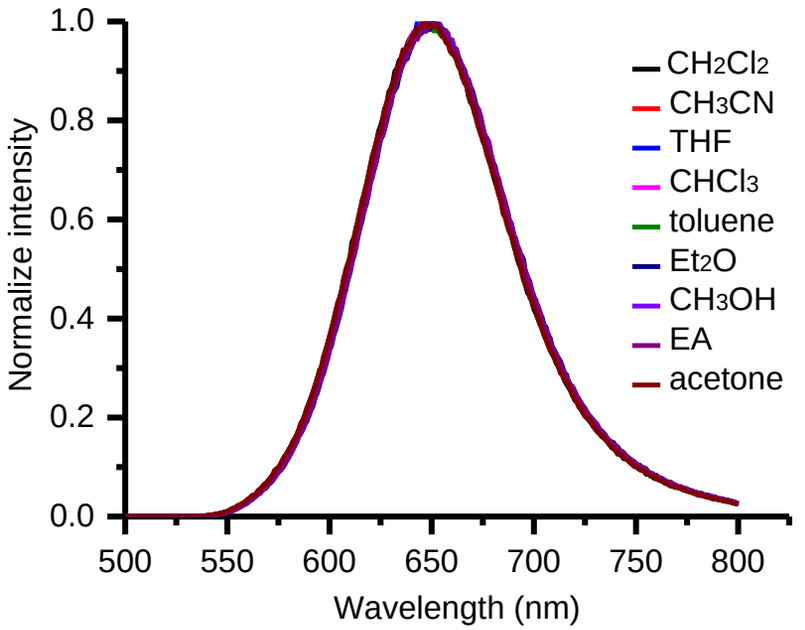

Fig. S35 Emission spectra of the PMMA film doped with 3% **1b** upon exposure to various vapours at ambient temperature.

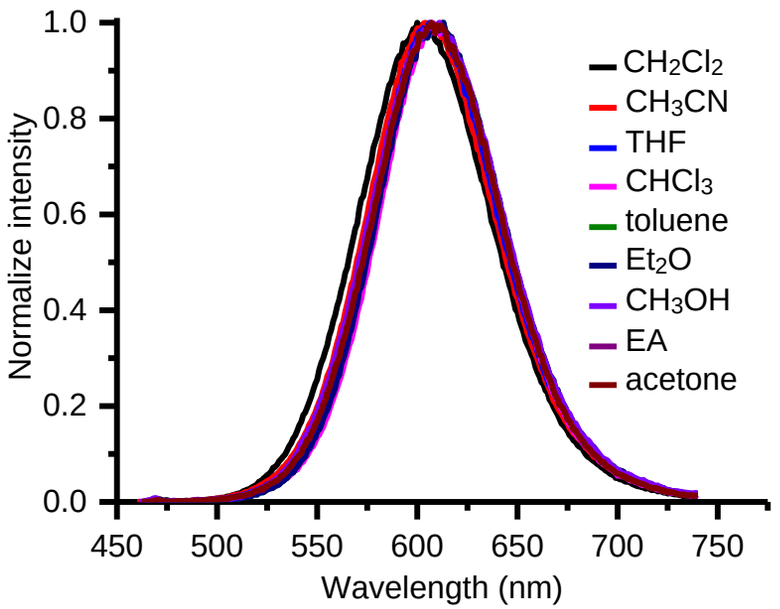

Fig. S36 Emission spectra of the PMMA film doped with 3% **3b** upon exposure to various vapours at ambient temperature.

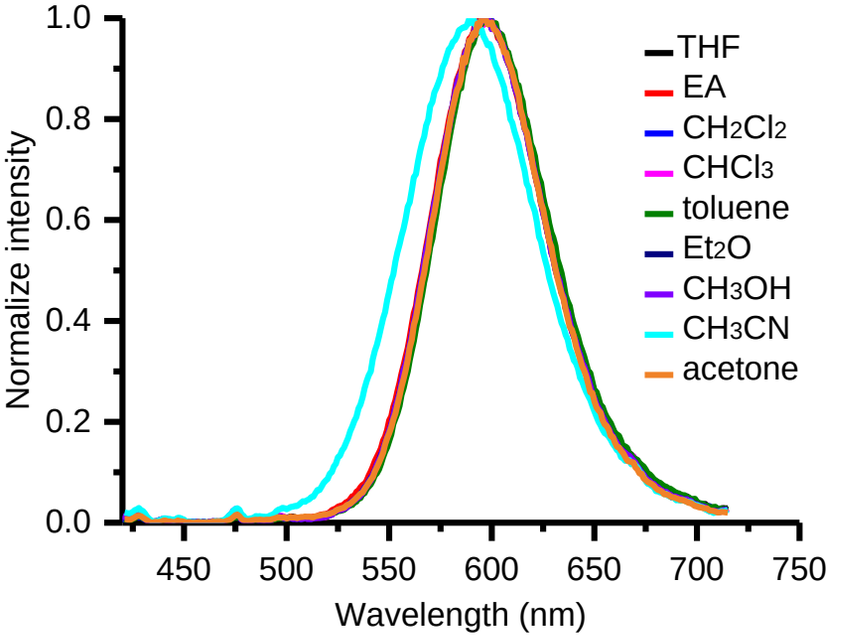

Fig. S37 Emission spectra of the PMMA film doped with 3% **4b** upon exposure to various vapours at ambient temperature.

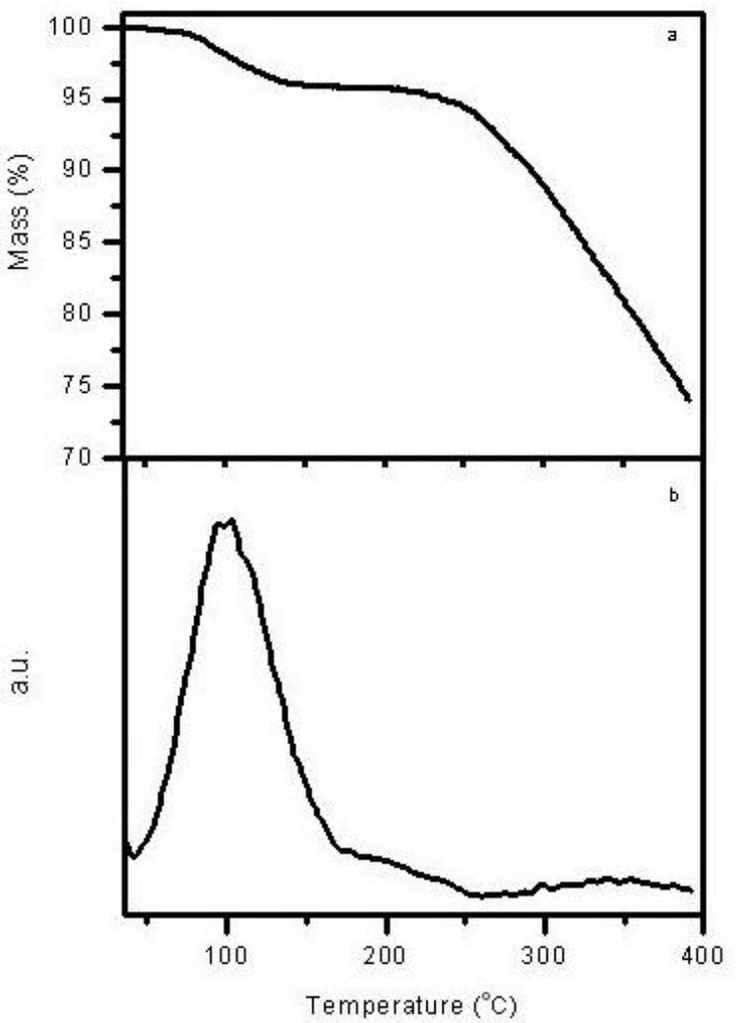

Fig. S38 Thermal gravitational curve (a) and quadrupole mass spectrometry (b) for crystalline sample **2b**·2.5MeCN showing weight loss of solvate MeCN.

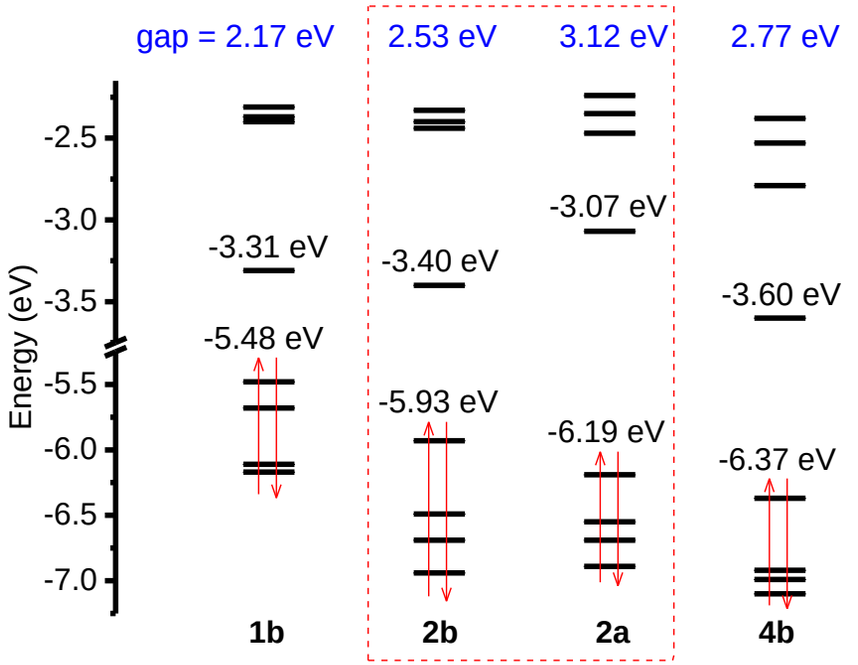

Fig. S39 Plots of energy level of frontier molecular orbitals in the lowest-energy triplet states for complexes **2a**, **1b**, **2b**, and **4b**, respectively, in the CH_2Cl_2 solution calculated by TD-DFT method at the B3LYP level.

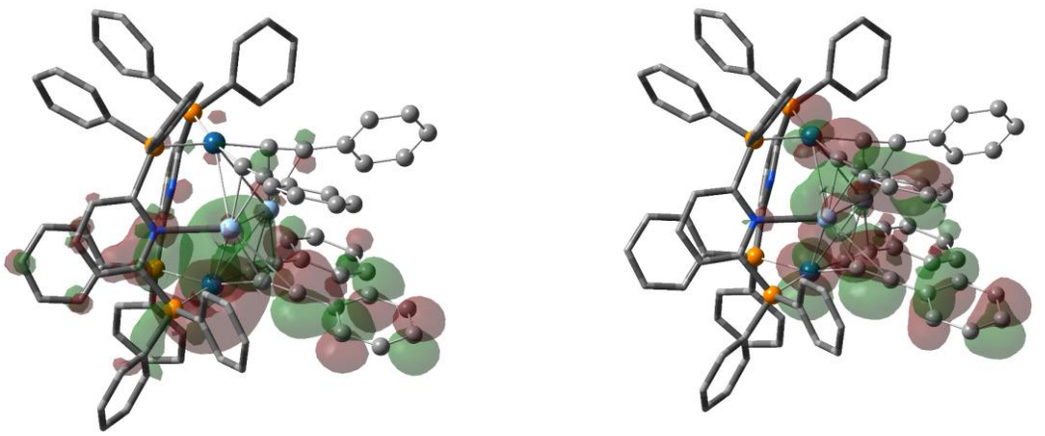

LUMO HOMO

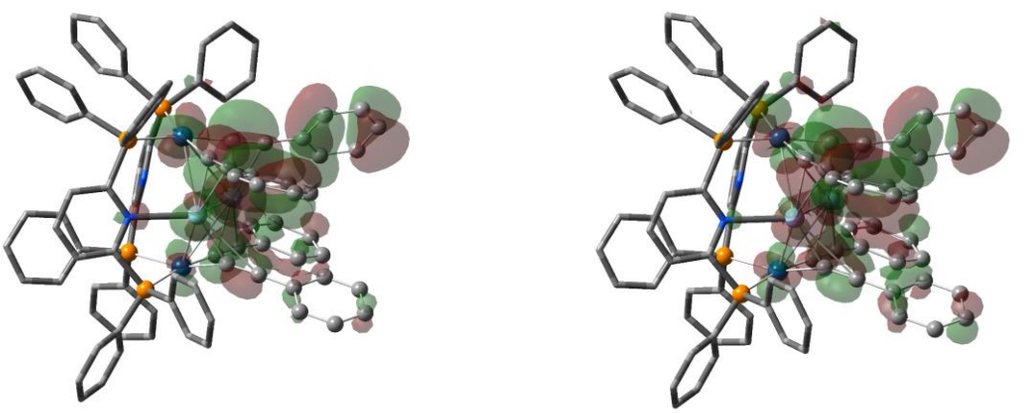

HOMO-1 HOMO-2

Fig. S40 Plots of the frontier molecular orbitals involved in the emission transition for complex **2a** by TD-DFT method at the B3LYP level (isovalue = 0.02).

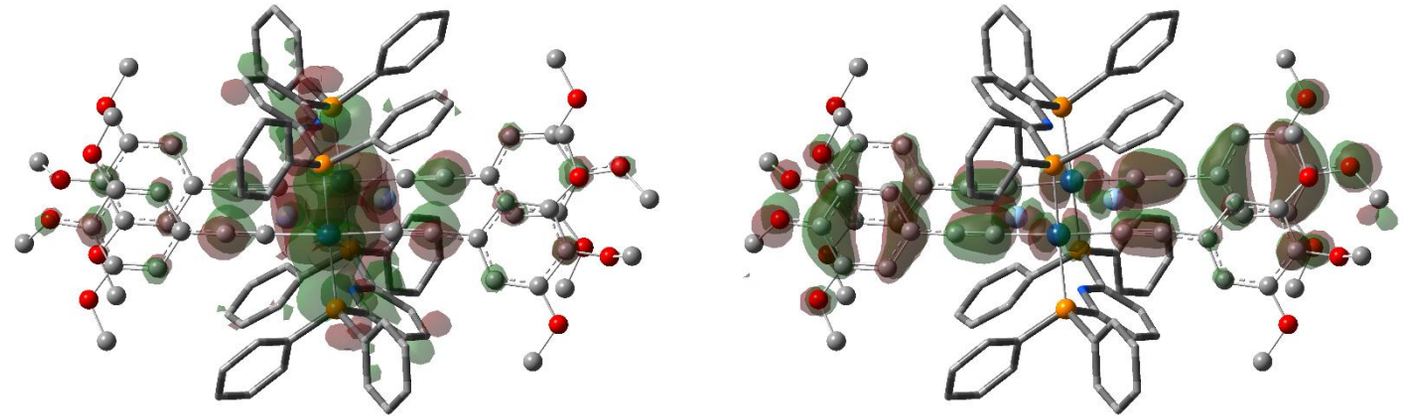

LUMO HOMO

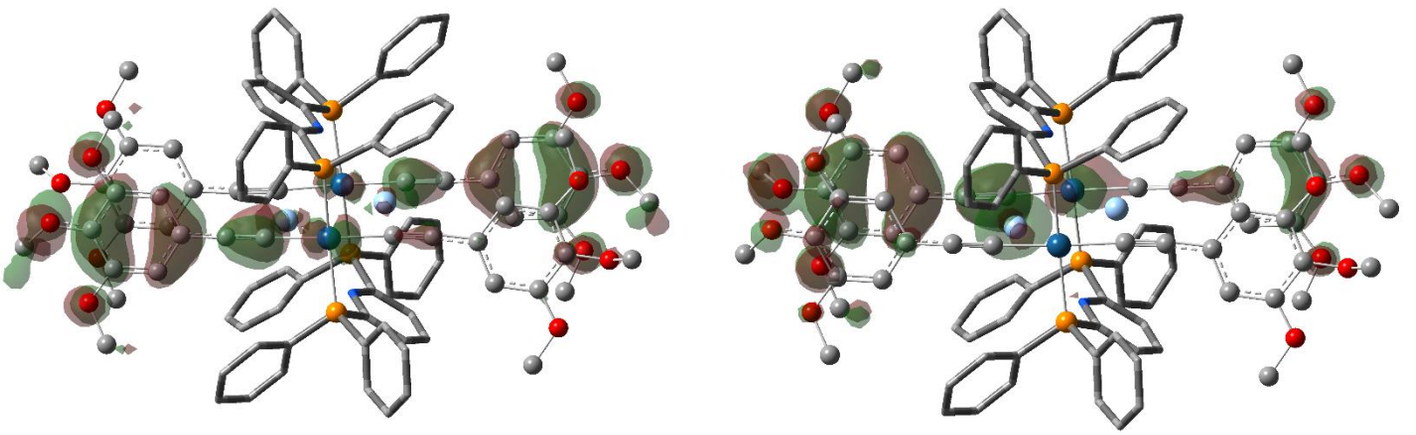

HOMO-1 HOMO-2

Fig. S41 Plots of the frontier molecular orbitals involved in the emission transition for complex **1b** by TD-DFT method at the B3LYP level (isovalue = 0.02).

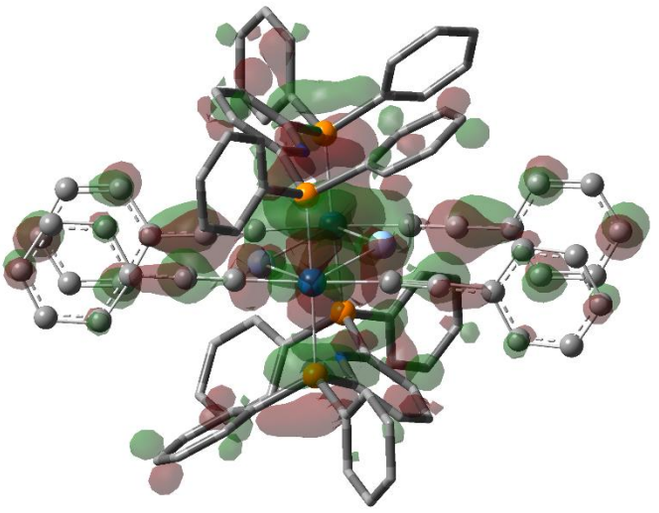

LUMO+1

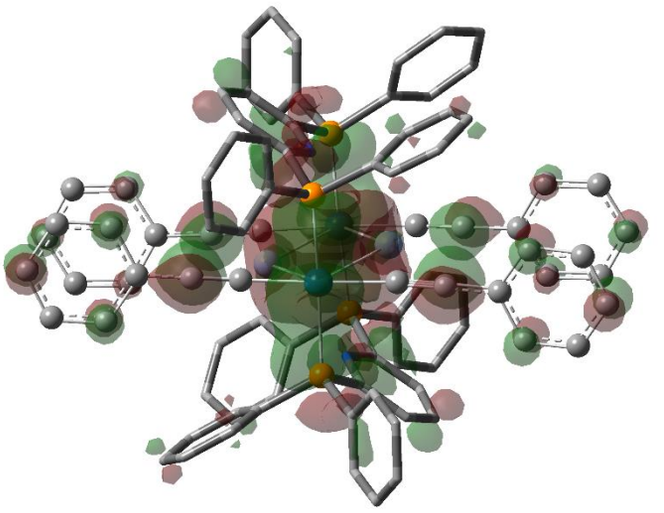

LUMO

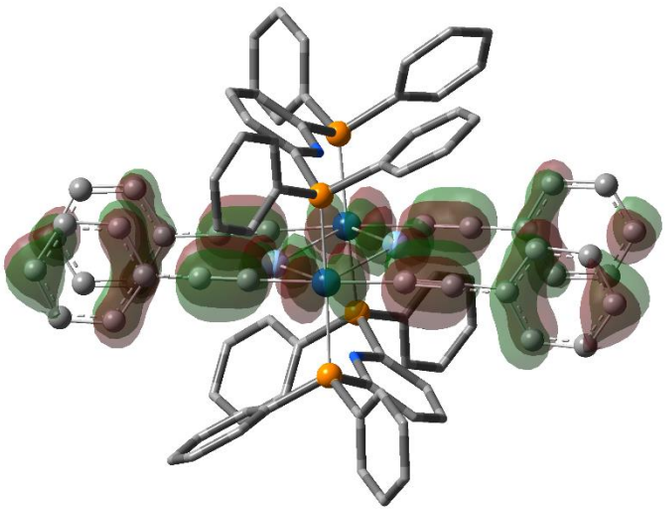

HOMO

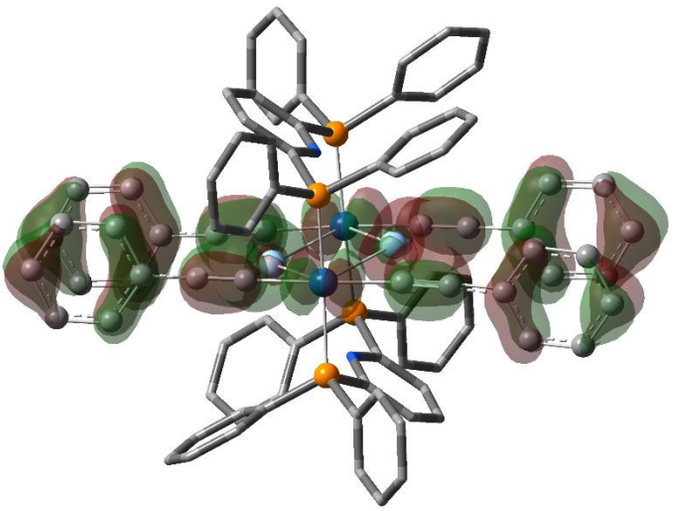

HOMO-1

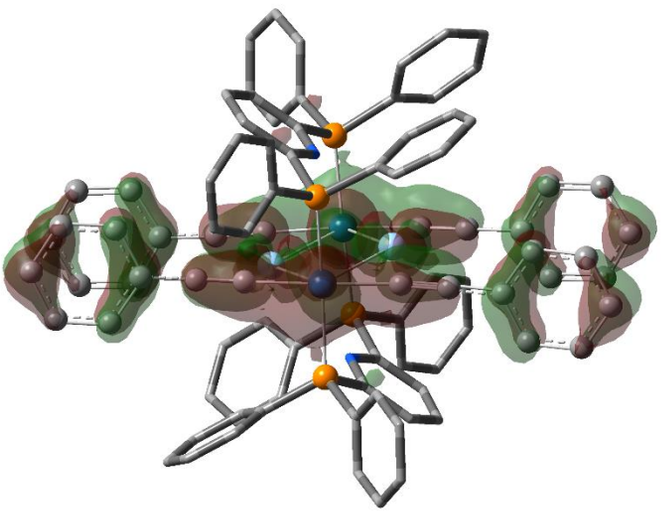

HOMO-2

Fig. S42 Plots of the frontier molecular orbitals involved in the emission transition for complex **2b** by TD-DFT method at the B3LYP level (isovalue = 0.02).

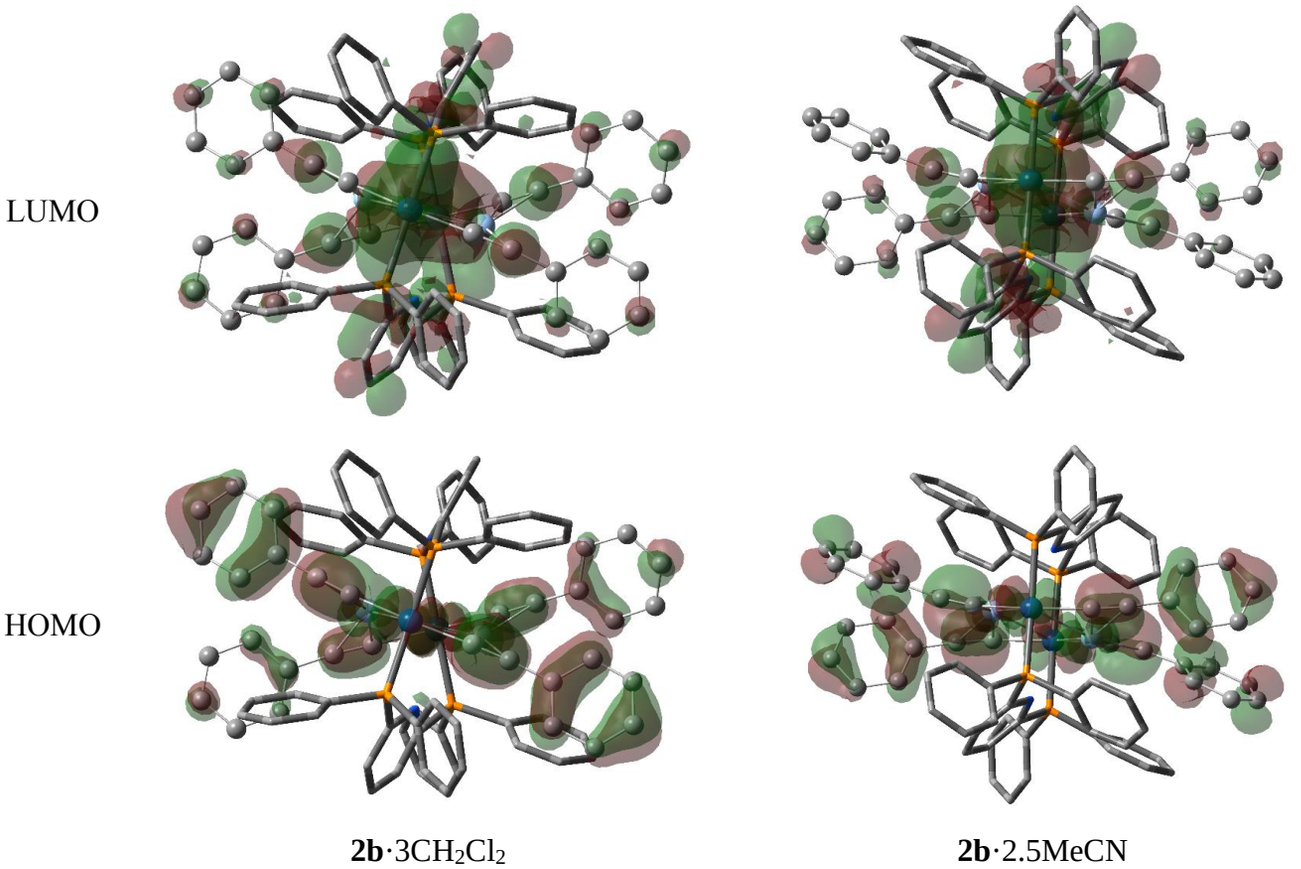

Fig. S43 Plots of the frontier molecular orbitals for **2b**·$3CH_2Cl_2$ and **2b**·2.5MeCN in the crystal states calculated by TD-DFT Method at the B3LYP Level (isovalue = 0.02).

References

1 D. Reddy, D. Jaganyi, *Dalton. Trans.*, 2008, 6724.

2 J. Benito, J. R. Berenguer, J. Forniés, B. Gil, J. Gómez, E. Lalinde, *Dalton. Trans.*, 2003, 4331.

3 R. Severin, J. Reimer, S. Doye, *J. Org. Chem.*, 2010, **75**, 3518.

4 G. M. Sheldrick, *SHELXL-97, Program for the Refinement of Crystal Structures*; University of Göttingen: Göttingen, Germany, **1997**.

5. M. J. Frisch, G. W. Trucks, H. B. Schlegel, G. E. Scuseria, M. A. Robb, J. R. Cheeseman, G. Scalmani, V. Barone, B. Mennucci, G. A. Petersson, H. Nakatsuji, M. Caricato, X. Li, H. P. Hratchian, A. F. Izmaylov, J. Bloino, G. Zheng, J. L. Sonnenberg, M. Hada, M. Ehara, K. Toyota, R. Fukuda, J. Hasegawa, M. Ishida, T. Nakajima, Y. Honda, O. Kitao, H. Nakai, T. Vreven, J. A. Montgomery, Jr., J. E. Peralta, F. Ogliaro, M. Bearpark, J. J. Heyd, E. Brothers, K. N. Kudin, V. N. Staroverov, T. Keith, R. Kobayashi, J. Normand, K. Raghavachari, A. Rendell, J. C. Burant, S. S. Iyengar, J. Tomasi, M. Cossi, N. Rega, J. M. Millam, M. Klene, J. E. Knox, J. B. Cross, V. Bakken, C. Adamo, J. Jaramillo, R. Gomperts, R. E. Stratmann, O. Yazyev, A. J. Austin, R. Cammi, C. Pomelli, J. W. Ochterski, R. L. Martin, K. Morokuma, V. G. Zakrzewski, G. A. Voth, P. Salvador, J. J. Dannenberg, S. Dapprich, A. D. Daniels, O. Farkas, J. B. Foresman, J. V. Ortiz, J. Cioslowski, D. J. Fox, *Gaussian 09*, *revision D.01*. Gaussian, Inc., Wallingford CT, 2013.

6. A. D. Becke, *J. Chem. Phys.*, 1993, **98**, 5648.

7. R. Bauernschmitt, R. Ahlrichs, *Chem. Phys. Lett.*, 1996, **256**, 454.

8. M. E. Casida, C. Jamorski, K. C. Casida, D. R. Salahub, *J. Chem. Phys.*, 1998, **108**, 4439.

9. R. E. Stratmann, G. E. Scuseria, M. J. Frisch, *J. Chem. Phys.*, 1998, **109**, 8218.

10. V. Barone, M. Cossi, J. Tomasi, *J. Chem. Phys.*, 1997, **107**, 3210.

11. M. Cossi, G. Scalmani, N. Rega, V. Barone, *J. Chem. Phys.*, 2002, **117**, 43.

12. D. Andrae, U. Häussermann, M. Dolg, H. Stoll, H. Preuss, *Theor. Chim. Acta.*, 1990, **77**, 123.

13. P. Ros, G. C. A. Schuit, *Theo. Chim. Acta (Berl.)*, 1966, **4**, 1.

14. T. Lu, F. W. Chen, *J. Comp. Chem.*, 2012, **33**, 580.